



## 저작자표시-비영리-변경금지 2.0 대한민국

이용자는 아래의 조건을 따르는 경우에 한하여 자유롭게

- 이 저작물을 복제, 배포, 전송, 전시, 공연 및 방송할 수 있습니다.

다음과 같은 조건을 따라야 합니다:



저작자표시. 귀하는 원저작자를 표시하여야 합니다.



비영리. 귀하는 이 저작물을 영리 목적으로 이용할 수 없습니다.



변경금지. 귀하는 이 저작물을 개작, 변형 또는 가공할 수 없습니다.

- 귀하는, 이 저작물의 재이용이나 배포의 경우, 이 저작물에 적용된 이용허락조건을 명확하게 나타내어야 합니다.
- 저작권자로부터 별도의 허가를 받으면 이러한 조건들은 적용되지 않습니다.

저작권법에 따른 이용자의 권리는 위의 내용에 의하여 영향을 받지 않습니다.

이것은 [이용허락규약\(Legal Code\)](#)을 이해하기 쉽게 요약한 것입니다.

[Disclaimer](#)

공학박사 학위논문

# **Processing and Numerical Simulation of Carbon Fiber Composites for Automotive Wheel**

탄소섬유 복합재료 차륜의 성형 및 수치 해석

2019년 8월

서울대학교 대학원

재료공학부

황 정 민

# Processing and Numerical Simulation of Carbon Fiber Composites for Automotive Wheel

탄소섬유 복합재료 차륜의 성형 및 수치 해석

지도 교수 윤 재 룬

이 논문을 공학박사 학위논문으로 제출함  
2019년 06월

서울대학교 대학원  
재료공학부  
황 정 민

황 정 민의 공학박사 학위논문을 인준함  
2019년 06월

위 원 장 \_\_\_\_\_ (인)

부위원장 \_\_\_\_\_ (인)

위 원 \_\_\_\_\_ (인)

위 원 \_\_\_\_\_ (인)

위 원 \_\_\_\_\_ (인)

Doctoral Dissertation in Engineering

**Processing and Numerical Simulation of  
Carbon Fiber Composites  
for Automotive Wheel**

by

Zheng Min Huang

Advisor: Prof. Jae Ryoun Youn

August 2019

Department of Materials Science and Engineering

Graduate School

Seoul National University

## **Abstract**

# **Processing and Numerical Simulation of Carbon Fiber Composites for Automotive Wheel**

Zheng Min Huang

Department of Materials Science and Engineering

The Graduate School

Seoul National University

In recent years, many studies have focused on improving material properties such as weight reduction, thermal/mechanical stability in the manufacturing industry. This can be achieved through several approaches: new structural design, processing, and materials. In particular, replacing existing heavy materials with lightweight materials can induce a big impact. Carbon fiber composites are emerging as a great alternative, and the research and demand for them is increasing dramatically. They are currently used in a wide range of industries, including aerospace, automotive, wind blade and sports. This study mainly dealt with carbon fiber composite automotive wheel manufacturing, one of the automotive components that can play an important role in reducing the weight of automobiles. The carbon fiber composite automotive wheel was manufactured with two typical polymer processing: Resin Transfer Molding (RTM) and Injection Molding (IM). In the RTM process, simulations were conducted first to predict the resin flow behavior and optimize the process conditions to fabricate final developed products that passed the vehicle test. In the IM process, three dimensional (3D) numerical analysis was carried out to investigate the resin flow and warpage of the product. The possibility of actual processing was also confirmed by fabricating the specimens. It provided a meaningful guideline for manufacturing a real automotive wheel via injection molding.

In Chapter 2, the entire process of manufacturing wheels by RTM process was described. At first, we studied the permeability tensor of the fiber preform. It is a key material property for satisfactory resin transfer molding process. The creeping flow simulation was carried out to obtain the flow field in a unit cell, and Darcy's law was utilized to compute the permeability tensor. The unit cell for the non-crimp fabrics (NCFs) was defined and constructed, and the permeability was analyzed in the axial, transverse, and thickness directions. The effect of shifted preform layers was also evaluated for more realistic permeability tensor. The predicted and measured results were compared with respect to the fiber volume fraction, fabric pattern, and stacking structure. And then, 3D numerical simulation was carried out to investigate the resin flow behavior in a complicated mold. A 19-inch automotive wheel rim was designed and fabricated using carbon fiber preform and epoxy resin. Case studies were performed to minimize the void formation during processing. It was found that the numerical and experimental results were in good agreement with each other, and the numerical optimization led to significant improvement in the quality of the product. Finally, thermal, mechanical, viscoelastic and structural analysis were performed to characterize the final developed wheel rim. The reliability of various properties has been improved by comparing benchmark wheel and reference values. As a result, a carbon fiber composite automotive wheel satisfying various criteria has been successfully developed and fabricated.

In Chapter 3, material design for producing the carbon fiber composite wheel among the thermoplastic resins was performed firstly. After the resin was selected as 40 wt% carbon fiber filled Polyamide 6 (PA6), injection molding of carbon fiber composite automotive wheels with complex shape was investigated numerically. As the geometry is not a common simple shape for injection molding, but a cylindrical complex shape, diaphragm gate was introduced and the size and shape of the sprue, gate and runner were specially designed. The resin flow during filling and deformation of parts after ejection were predicted numerically. The filling time in the cavity was optimized and the gate freezing time was determined. Insert injection molding was also considered to reduce the deformation of the part and improve the mechanical properties. The insert injection molded part was assessed in terms of pressure, fiber orientation, deformation, elastic modulus, and residual stress distribution. It was found that the deformation of the part

was significantly reduced when the insert was applied. In addition, the specimens were fabricated to show the possibility of real manufacturing processing. The same characterization with RTM products such as thermal, mechanical and viscoelastic analysis were measured. The manufacturing possibility of actual injection molding process was verified by comparison with product manufactured by RTM.

**Keywords:** Carbon fiber composite, Automotive wheel, Resin Transfer Molding, Permeability, Shifting effect, Void formation, Numerical simulation, Injection Molding, Warpage deformation, Thermal residual stress

**Student Number:** 2013-22473

# Contents

Abstract.....	i
List of Figures .....	vi
List of Tables.....	ix
 <b>Chapter 1. Introduction .....</b>	<b>1</b>
1.1. Carbon fiber composites .....	1
1.2. Research background.....	3
1.2.1. Resin Transfer Molding .....	3
1.2.2. Injection Molding.....	4
1.3. Objectives of present work .....	7
1.4. References .....	8
 <b>Chapter 2. Resin Transfer Molding.....</b>	<b>9</b>
2.1. Analysis of preform permeability .....	9
2.1.1. Introduction.....	9
2.1.2. Numerical analysis.....	11
2.1.3. Experimental section.....	16
2.1.4. Results and discussion .....	18
2.1.5. Summary .....	29
2.1.6. References.....	30
2.2. Numerical simulation and processing.....	32
2.2.1. Introduction.....	32
2.2.2. Numerical analysis.....	34
2.2.3. Experimental section.....	41
2.2.4. Results and discussion .....	42
2.2.5. Summary .....	49



2.2.6. References.....	50
2.3. Product properties measurements.....	52
2.3.1. Introduction.....	52
2.3.2. Experimental section.....	54
2.3.3. Results and discussion .....	56
2.3.4. Summary.....	64
2.3.5. References.....	65
<b>Chapter 3. Injection Molding .....</b>	<b>66</b>
3.1. Material design.....	66
3.1.1. Selection criteria .....	66
3.1.2. Summary.....	70
3.1.3. References.....	71
3.2. Numerical simulation.....	72
3.2.1. Introduction.....	72
3.2.2. Numerical analysis.....	73
3.2.3. Results and discussion .....	79
3.2.4. Summary.....	88
3.2.5. References.....	89
3.3. Specimen production and characterization .....	91
3.3.1. Introduction.....	91
3.3.2. Experimental section.....	92
3.3.3. Results and discussion .....	95
3.3.4. Summary.....	101
3.3.5. References.....	102
<b>Korean Abstract .....</b>	<b>103</b>

# List of Figures

<b>Fig. 1.2.1.</b> Schematic illustration of Resin Transfer Molding process .....	5
<b>Fig. 1.2.2.</b> Schematic illustration of Injection Molding process.....	6
<b>Fig. 2.1.1.</b> Carbon fiber NCFs used in this study. Photographs of (a) front side and (b) back side for the NCF 0°. (c) Front image and (d) back image of modeled geometry for the NCF 0°. Photographs of (e) front side and (f) back side for the NCF ±45°. (g) Front image and (h) back image of modeled geometry for the NCF ±45° ...	13
<b>Fig. 2.1.2.</b> Geometry and 3D mesh for unit cells of the NCF 0° and NCF ±45° without (a, c) and with (b, d) shifting. ....	14,15
<b>Fig. 2.1.3.</b> Schematic illustration of the mold used for the measurement of (a) in-plane and (b) out-of-plane permeability.....	20
<b>Fig. 2.1.4.</b> Experimental set-up for the measurement of (a, b) in-plane and (c, d) out-of-plane permeability.....	21
<b>Fig. 2.1.5.</b> Velocity profile and pressure field without shifting effect for (a) NCF 0° and (b) NCF ±45° .....	22
<b>Fig. 2.1.6.</b> Velocity profile and pressure field with shifting effect for (a) NCF 0° and (b) NCF ±45° .....	23
<b>Fig. 2.1.7.</b> Advancement of the resin flow front for (a) NCF 0° ( $V_f = 61\%$ ) and (b) NCF ±45° ( $V_f = 69.6\%$ ) .....	25
<b>Fig. 2.1.8.</b> Linear fitting of the flow front for the NCF 0° in (a) the axial and (b) the transverse directions.....	26
<b>Fig. 2.1.9.</b> Comparison of the measured and predicted permeability of (a) NCF 0° and (b) NCF ±45° .....	28
<b>Fig. 2.2.1.</b> (a) Schematic illustration and (b) photographs of the mold and the CFRP .....	33
<b>Fig. 2.2.2.</b> Overall geometry and magnified cross-section of the CFRP rim: (a~d) for Case 1 and (e~h) for Case 4.....	37
<b>Fig. 2.2.3.</b> Photographs of the NCF used in this study. (a) Front side and (b) back side for the NCF 0°. (c) Front side and (d) back side for the NCF ±45° .....	38
<b>Fig. 2.2.4.</b> Local and global coordinates: $e_1$ , $e_2$ , and $e_3$ indicate axial, transverse, and thickness directions in the local coordinate, respectively.....	40
<b>Fig. 2.2.5.</b> Geometry and macro-void content of the CFRP rims .....	44

<b>Fig. 2.2.6.</b> Numerical results of the flow front: (a~d) for Case 1 and (e~g) for Case 4.....	45
<b>Fig. 2.2.7.</b> Filling percentage as a function of the time .....	46
<b>Fig. 2.2.8.</b> Overall and magnified cross-sectional views of the macro-void content calculated numerically: (a~d) for Case 1 and (e~h) for Case 4 .....	47
<b>Fig. 2.2.9.</b> (a) Photograph of the sectioned parts from the produced wheel rim. (b) Dimensional details of the specimen for Micro-CT. Images of voids in the wheel rim: (b) for Case 1 and (c) for Case 4. ....	48
<b>Fig. 2.3.1.</b> DSC results of the DR product and BM product .....	58
<b>Fig. 2.3.2.</b> Thermal conductivity of the DR product and BM product.....	59
<b>Fig. 2.3.3.</b> Stress-strain curves of the DR product and BM product for tensile test .....	60
<b>Fig. 2.3.4.</b> DMA results of the DR product and BM product .....	61
<b>Fig. 2.3.5.</b> Micro-CT images of the (a) BM product, (b) DR product (before improvement) and (c) DR product (after improvement).....	62
<b>Fig. 3.1.1.</b> Engineering plastics concept map.....	68
<b>Fig. 3.1.2.</b> Tensile properties as a function of carbon fiber weight fraction.....	69
<b>Fig. 3.2.1.</b> (a) Automotive wheel considered in this study, (b) CAD model, (c) finite element mesh, and (d) magnified mesh structure.....	75
<b>Fig. 3.2.2.</b> Geometry of (a) runner and gate, (b) cooling channel, and (c) mold.....	76
<b>Fig. 3.2.3.</b> Geometry of (a) Case 1 without insert and (b) Case 2 with insert. ....	77
<b>Fig. 3.2.4.</b> Sprue pressure w.r.t. the filling time .....	81
<b>Fig. 3.2.5.</b> Existing polymer melt w.r.t. time: (a) Case 1 and (b) Case 2 .....	82
<b>Fig. 3.2.6.</b> Melt front advancement in the cavity w.r.t. time: (a) Case 1 and (b) Case 2 at 25%, 75%, and 100% filling.....	83
<b>Fig. 3.2.7.</b> Pressure distribution after 100% filling: (a) Case 1, (b) Case 2, (c) Comparison of the total weight between the two cases .....	84
<b>Fig. 3.2.8.</b> Fiber orientation at the skin layer: (a) Case 1 and (b) Case 2.....	85
<b>Fig. 3.2.9.</b> Elastic modulus of the molded part in the x, y and z direction: (a) Case 1 and (b) Case 2.....	86
<b>Fig. 3.2.10.</b> Total deformation and thermal residual stress of the molded part for Case 1 ((a) and (c)) and Case 2 ((b) and (d)).....	87
<b>Fig. 3.3.1.</b> Experimental progress for fabrication of PA/40CF specimen .....	93

<b>Fig. 3.3.2.</b> PA/40CF and PA specimens by injection molding.....	96
<b>Fig. 3.3.3.</b> DSC results of PA/40CF and pure PA specimens .....	97
<b>Fig. 3.3.4.</b> TGA results of PA/40CF and pure PA specimens .....	98
<b>Fig. 3.3.5.</b> Stress-strain curves of the PA/40CF and pure PA specimens for tensile test.....	99
<b>Fig. 3.2.6.</b> DMA results of the PA/40CF and pure PA specimens. ....	100

## List of Tables

<b>Table 2.1.1.</b> Permeability predicted for (a) NCF 0° and (b) NCF ±45° .....	24
<b>Table 2.1.2.</b> Permeability measured for (a) NCF 0° and (b) NCF ±45° .....	27
<b>Table 2.2.1.</b> Fiber volume fraction and permeability of the NCFs used in this study .....	39
<b>Table 2.3.1.</b> Calculated porosity results of BM product, DR product (before improvement) and DR product (after improvement). .....	63
<b>Table 3.2.1.</b> Process conditions used in the simulation. ....	78
<b>Table 3.3.1.</b> Process conditions for the experiments. ....	94

# Chapter 1.

## Introduction

### 1.1. Carbon fiber composites

A composite material is a combination of two or more kinds of different materials, which has characteristics that cannot be obtained by a single material. It is typically composed of matrix and reinforced materials. Since the carbon fiber composite is a kind of composite materials, it has the same composition. The carbon fiber composite is classified into plastic (Carbon Fiber Reinforced Plastic, CFRP), carbon (Carbon Fiber Reinforced carbon, C/C), ceramic (Carbon Fiber Reinforced Ceramic, CFRC) and metal (Carbon Fiber Reinforced Metal, CFRM) by matrix. Among them, CFRP is the main type and becoming commercialized. It is also classified as thermosetting resin (Carbon Fiber Reinforced Thermosetting, CFRTS) and thermoplastic resin (Carbon Fiber Reinforced Thermoplastic, CFRTTP) by a matrix resin <sup>1-3</sup>. For thermosets, epoxy resins were generally used. As a processing method, the RTM process is used to impregnate low-molecular resin on a carbon fabric, and then the temperature is increased to form a cross-linking within the resin. For thermoplastics, nylon and polycarbonate resins are used. The processing method is an injection molding that the milled carbon fiber is compounded with the resin, extruded it into a pellet, and then injected into a desired product shape.

Long carbon fiber reinforced plastics exhibit anisotropic properties such as mechanical, thermal and electrical properties that are significantly different from those of longitudinal direction and transverse direction. This is a typical feature of fiber reinforced composite materials <sup>4</sup>. The fiber direction and its amount should be designed according to the required properties <sup>5</sup>. The tensile, bending, and compressive properties of the longitudinal direction are determined by the strength and elastic modulus of the fiber. While, the tensile, bending, compressive and shear properties in the perpendicular direction are mainly controlled by the resin and the interface between resin and fiber.

Therefore, the tensile strength and elastic modulus in the longitudinal direction are generally shown as values considering the tensile strength of the fiber and the fiber volume fraction, and the properties of the transverse direction are almost determined by the resin <sup>6-8</sup>. In the case of short fiber reinforced plastic, it is possible to processing in various methods, and the production cost is reduced due to mass consumption <sup>9</sup>. When compared to glass fiber, carbon fiber gives plastic functionality such as electrical conductivity, abrasion resistance, and thermal conductivity in addition to its mechanical property, so the expectation for application as a functional composite material is very high. As such a short-fiber reinforced plastic, various thermoplastic resins are used as a matrix <sup>10, 11</sup>.

## 1.2. Research background

### 1.2.1. Resin Transfer Molding

Resin Transfer Molding (RTM) is a method of placing a fabric in a mold cavity in advance and filling it with a low viscosity thermosetting resin. It is an attractive process because it has great potential to produce complicated polymer composites with good surface quality and dimensional stability<sup>12, 13</sup>. It includes several steps, such as preforming, impregnation, curing, and ejection as shown in **Fig. 1.2.1**.

In the 1930s, an early form of RTM defined as the Marco process was introduced to production of large symmetrical moldings such as boats<sup>14</sup>. In the 1960s, a study was carried out to inject metal matrix into oriented fiber preforms<sup>15</sup>. This is a variant of RTM, which mostly uses polymers as a matrix. After that time, the RTM process was used for the production of advanced composites using polymer matrix. It was used for components such as aeroengine compressor blades in the late 1970s. These early products require a high level of geometric accuracy, which is still an influence on the development of many RTM components. By 1980, many researchers had tried to find a new processing method that could break through the limitations of existing aerospace manufacturing processes<sup>16</sup>. Recently, the RTM process has been applied to various industrial composites such as aerospace parts, automotive components, and wind blades<sup>17, 18</sup>.

Studies on RTM process simulation are mainly carried out on the filling stage. The simulation results are very helpful to confirm the actual process conditions. For example, by predicting the resin flow behavior, it can be determined filling state and void formation. In addition, the inlet and vent locations of resin can be optimized before the actual mold fabrication, and which can reduce the costs and time.

The RTM process simulation was initially considered as isothermal conditions. However, methods like preheated molds and resins used in actual process have been applied to the simulation, so it is carried out under non-isothermal temperature conditions. Because this paper mainly described the resin flow pattern and void formation during the filling stage, the temperature is set to a constant value.



### 1.2.2. Injection Molding

The injection molding process is a molding method in which a plastic material is melted by a heater in a cylinder of an injection molding machine and pressed into the mold with a pressurizing plunger. It is one of the most diverse and important manufacturing processes, enabling mass production of complex plastic parts with high dimensional tolerances. As the quality and yield requirements of parts are becoming more stringent, injection molding processes and quality control have been studied in many years<sup>19, 20</sup>.

In 1872, Hyatt and his brother Isaiah patented the first plastic injection molding machine. The machine was relatively simple compared to machines in use today. It worked like a large hypodermic needle, using a plunger to inject plastic through a heated cylinder into a mold. The industry progressed slowly over the years, producing small products such as collar stays, buttons, and combs.

American inventor James Watson Hendry created the first screw injection machine that could control the speed and quality of plastic injections much better in 1946. The machine also allowed material to be mixed before injection, so that colored or recycled plastic could be added to virgin material and mixed completely before being injected. Affected by that, most injection machines are manufactured in screw type currently<sup>21, 22</sup>.

Procedure for injection molding process is as shown in **Fig. 1.2.2**. First, the plastic is heated and melted, and then the melted plastic is sent forward with a screw. Next, move the screw forward and push the melted plastic into the cavity of the mold through the nozzle with high pressure. When the plastic is hardened in the mold, open the mold and take the product out. At this time, the mold is cooled during the molding of thermoplastics. Since the temperature is less than that of the thermoplastics used for processing, the mold may be heated with water or oil. Thus, a very complicated process is automatically and continuously used on one machine.

The cycle of injection molding, which is usually only a few seconds, and more than a minute is limited to being large and extremely thick. The example of plastic products with injection molds is so many different fields that it is impossible to sort them out. It can be molded from very small ones to large ones up to 10 kg in weight, and can be mass-produced by repeated injection, thus improving work efficiency.

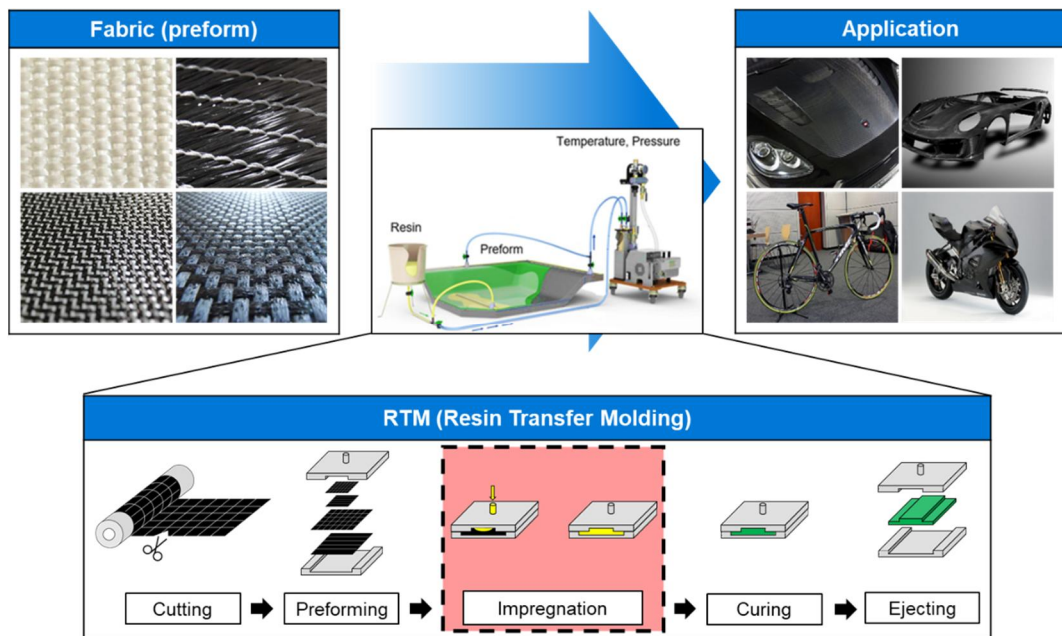


**Figure 1.2.1.** Schematic illustration of Resin Transfer Molding process.

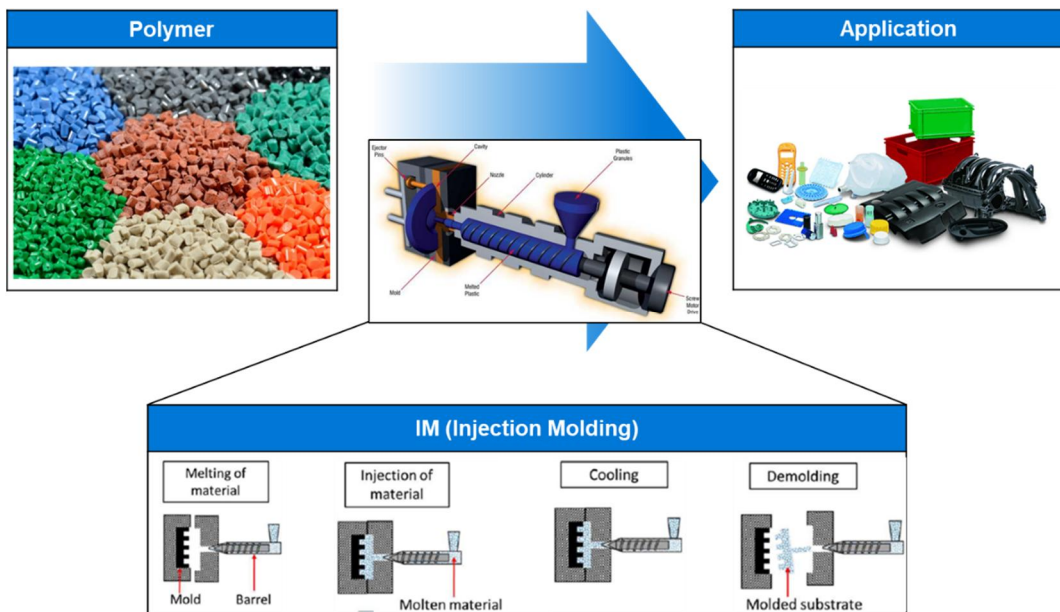


**Figure 1.2.2.** Schematic illustration of Injection Molding process.

### 1.3. Objectives of present work

The main objectives of this study are to fabricate a carbon fiber composite automotive wheel. It was manufactured with Resin Transfer Molding (RTM) and Injection Molding (IM).

In Chapter 2, the RTM process of manufacturing wheels was developed. At first, the permeability tensor of fiber preform was predicted and measured, which is one of the key material properties for satisfactory resin transfer molding process. The unit cell for the non-crimp fabrics (NCFs) was defined and constructed, and the permeability was analyzed in the axial, transverse, and thickness directions. The shifting effect was also considered for more realistic permeability tensor in numerical analysis. After the permeability was measured by two measurements, comparison between predicted and measured results were performed with respect to the fiber volume fraction, fabric pattern, and stacking structure. And then, 3D numerical simulation was carried out to investigate the resin flow behavior in an automotive wheel rim. Processing optimization was performed to minimize the void formation. Several measurements such as thermal, mechanical, viscoelastic and structural analysis were performed to characterize the final developed wheel rim. The reliability of various properties has been improved by comparing benchmark wheel and reference values.

In Chapter 3, material design for manufacturing the carbon fiber composite wheel among the thermoplastic resins was performed firstly. After selection of the resin, injection molding of carbon fiber composite automotive wheels was investigated numerically. The resin flow during filling and deformation of parts after ejection were predicted numerically. Insert injection molding was also considered to reduce the deformation of the part and improve the mechanical properties. In addition, the specimens were fabricated to show the possibility of real manufacturing processing. The same characterization with RTM products such as thermal, mechanical and viscoelastic analysis were performed.

## 1.4. References

1. Chung, D. D.; Chung, D., *Carbon fiber composites*. Elsevier: 2012.
2. Margolis, J., *Engineering plastics handbook*. McGraw Hill Professional: 2005.
3. Chand, S., Review carbon fibers for composites. *Journal of materials science* **2000**, 35 (6), 1303-1313.
4. Agarwal, B. D.; Broutman, L. J.; Chandrashekhara, K., *Analysis and performance of fiber composites*. John Wiley & Sons: 2017.
5. Mallick, P. K., *Fiber-reinforced composites: materials, manufacturing, and design*. CRC press: 2007.
6. Edie, D., The effect of processing on the structure and properties of carbon fibers. *Carbon* **1998**, 36 (4), 345-362.
7. Edwards, K., An overview of the technology of fibre-reinforced plastics for design purposes. *Materials & design* **1998**, 19 (1-2), 1-10.
8. Hyer, M. W.; White, S. R., *Stress analysis of fiber-reinforced composite materials*. DEStech Publications, Inc: 2009.
9. Sheikh-Ahmad, J. Y., *Machining of polymer composites*. Springer: 2009; Vol. 387355391.
10. Deve, H. E.; McCullough, C., Continuous-fiber reinforced composites: A new generation. *Jom* **1995**, 47 (7), 33-37.
11. Hollaway, L., *Handbook of polymer composites for engineers*. Elsevier: 1994.
12. Rudd, C. D.; Long, A. C.; Kendall, K.; Mangin, C., *Liquid moulding technologies: Resin transfer moulding, structural reaction injection moulding and related processing techniques*. Elsevier: 1997.
13. Rosato, D. V.; Rosato, D. V., *Reinforced plastics handbook*. Elsevier: 2004.
14. Mountfield, J., Forming processes for glass fibre and resin—other methods. *Composites* **1969**, 1 (1), 41-49.
15. Cooper, G., Forming processes for metal-matrix composites. *Composites* **1969**, 1 (2), 153-159.
16. Potter, K., *Resin transfer moulding*. Springer Science & Business Media: 2012.
17. Robertson, F. C., Resin transfer moulding of aerospace resins—a review. *British polymer journal* **1988**, 20 (5), 417-429.
18. Dutton, A.; Bonnet, P.; Hogg, P.; Lleong, Y., Novel materials and modelling for large wind turbine blades. *Proceedings of the Institution of Mechanical Engineers, Part A: Journal of Power and Energy* **2010**, 224 (2), 203-210.
19. Agrawal, A.; Pandelidis, I.; Pecht, M., Injection molding process control—A review. *Polymer Engineering & Science* **1987**, 27 (18), 1345-1357.
20. Chen, Z.; Turng, L. S., A review of current developments in process and quality control for injection molding. *Advances in Polymer Technology: Journal of the Polymer Processing Institute* **2005**, 24 (3), 165-182.
21. RAJI, A.; ATTAH, J. D.; OSSAI, C. D., Development of a portable laboratory injection moulding machine. *Leonardo Electronic Journal of Practices and Technologies* **2014**, (25), 10-25.
22. Saechtling, H. J., *International plastics handbook for the technologist, engineer and user*. Hanser: 1987.

# Chapter 2.

## Resin Transfer Molding

### 2.1. Analysis of preform permeability

#### 2.1.1. Introduction

The permeability of preforms, an indicator of textile materials to transmit fluids, plays an important role in the RTM process, particularly the resin impregnation step. Many methods have been investigated to obtain the permeability from analytical calculation, numerical prediction, and experimental measurement. Basically, the permeability is defined by Darcy's law that describes the fluid flow through a porous medium. One of the most popular analytical models is the Kozeny-Carman (KC) equation, which has been developed for granular beds with ellipsoidal shape <sup>1</sup>. Since then, a large number of analytical studies have been carried out, but most of them were for unidirectional fiber structures. Also, many numerical studies have been reported. For instance, Sangani and Acrivos numerically analyzed flows in the axial and transverse directions for square and hexagonal packing arrays of filaments <sup>2</sup>. Gebart calculated the permeability by considering different fiber packing and compared with the approximate analytical solution <sup>3</sup>. In addition, simplified models were proposed to predict the permeability of plain-woven fabric by using homogenization method <sup>4-7</sup>. The models using a rectangular unit cell assumed the Stokes equation and the Brinkman equation for inter-tow and intra-tow regions, respectively. However, these methods require an ideally aligned fiber structure, which is not realistic in composite manufacturing.

Recently, much research on carbon non-crimp fabrics (NCFs) has been conducted because of their high performance <sup>8-11</sup>. Due to the absence of crimping and through-thickness stitching, they have better in-plane mechanical properties and formability than common fabrics with a crimp structure. However, during the lay-up step of the RTM

process, the shifting between two adjacent stacking layers necessarily happens, which results in the blocking and nesting phenomena of fiber tows within the fabrics. Therefore, addressing these effects with a real stacking architecture is a very important issue in numerical simulation.

In this study, the permeability tensor was calculated for three-dimensional NCF fabrics by using homogenization method, which is implemented based on finite element method (FEM). For numerical analysis, creeping flow was adopted in the in-plane and out-of-plane directions. We also considered the shifting effect between two layers to take into account more realistic textile architecture. Radial and out-of-plane flow tests were performed to measure the relevant permeabilities. Comparison between the predicted values and the measured values were made with respect to the fiber volume fraction, fabric pattern, and stacking structure.

### 2.1.2. Numerical analysis

The homogenization method used in this study is a computational approach that can replace a heterogeneous material with an equivalent homogeneous material holding the same average properties at both microscale and macroscale<sup>12-16</sup>. Consequently, it has been widely applied to predict physical properties of materials. In the current study, a rectangular unit cell of the NCF fabrics was extracted for the homogenization, and the Stokes equation was calculated for flow. After the velocity field was computed, Darcy's law was used to calculate permeability. The periodic boundary condition was imposed in order to satisfy the periodicity of the unit cell.

#### 2.1.2.1. Governing equation

The flow field was obtained by using a commercial finite element software, Comsol Multiphysics<sup>®</sup>. It was assumed that the resin was an incompressible Newtonian fluid, and the fiber bundle was regarded as an impermeable solid. The governing equations are the continuity equation (Eq. 2.1.1) and the momentum equation, i.e., the Stokes equation (Eq. 2.1.2).

$$\nabla \cdot \mathbf{u} = 0 \quad (2.1.1)$$

$$\nabla P = \mu \nabla^2 \mathbf{u} \quad (2.1.2)$$

, where  $\mathbf{u}$  is the velocity vector of fluid,  $\mu$  is the Newtonian viscosity of fluid, and  $\nabla P$  is the pressure gradient vector.

#### 2.1.2.2. Geometric modeling

Real images and geometrical structures of the carbon fiber NCFs used in this study are



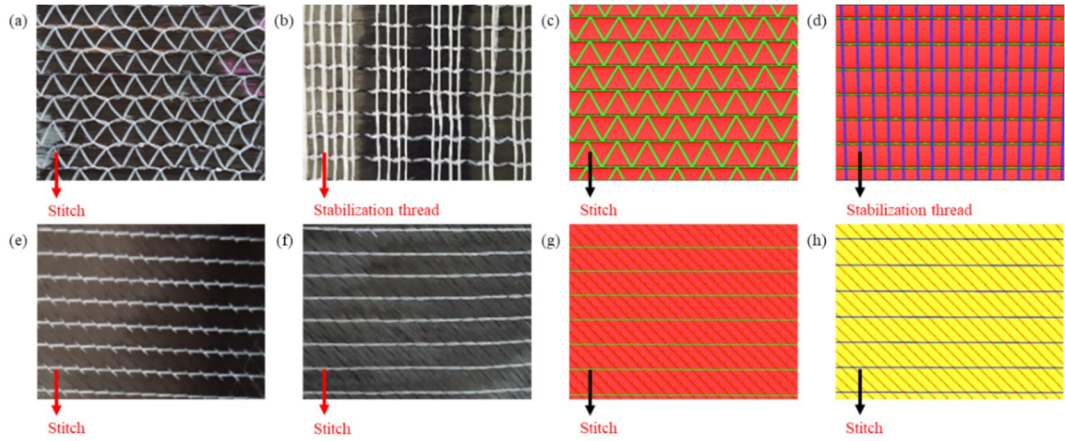
shown in **Fig. 2.1.1**. Domains of the unit cell with different scales are shown in **Fig. 2.1.2**. The mesoscale unit cell was extracted from the macroscale unit cell, and the different mesoscale unit cells were used to predict in-plane and out-of-plane permeabilities. For NCF 0°, the stitch fiber and stabilization thread were considered completely in in-plane direction. However, when the resin flows in out-of-plane direction, the fabrics were compressed in thickness direction during the experiment, the stitch fibers at the top and the stabilization thread at the bottom were also compressed and deformed. Therefore, stitch fibers only in the middle were considered for the flow analysis. For NCF 45°, all the stitch fibers were neglected since the size of the stitch fiber is smaller than that in the NCF 0°. It was assumed that the fiber bundles in the unit cell were in contact with one another. The fabric shifting effect between the layers during fabric stacking was considered in the flow analysis for more realistic modeling.

### 2.1.2.3. Flow Analysis for Unit Cell

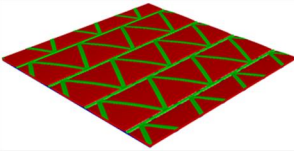
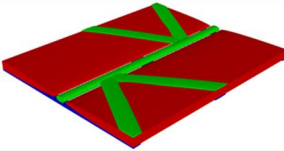
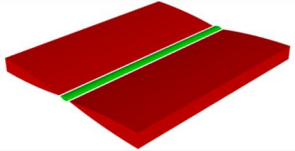
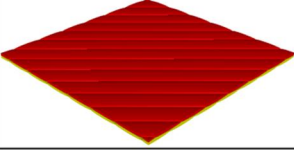
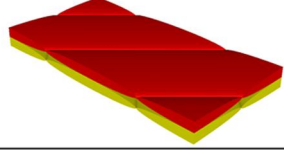
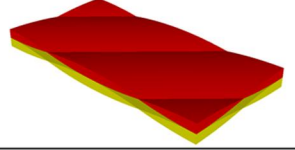
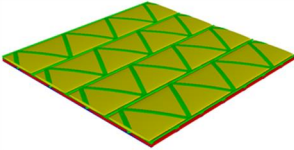
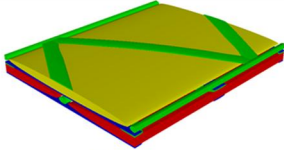
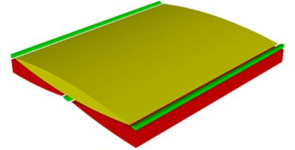
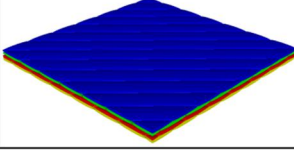
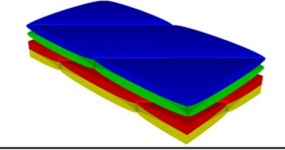
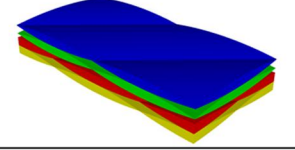
Pressure values were imposed as an inlet condition along the axial, transverse, and thickness directions. Periodic flow conditions were applied along the boundary of the unit cell. By using the numerical method described above, velocity profile and pressure field were computed, and then the total flow rate  $Q$  in each direction was calculated. The permeability for each direction ( $K_{xx}$ ,  $K_{yy}$ , and  $K_{zz}$ ) was obtained by using the following Darcy's equation (**Eq. 2.1.3**).

$$\mathbf{K} = \frac{Q\mu}{A\nabla P} \quad (2.1.3)$$

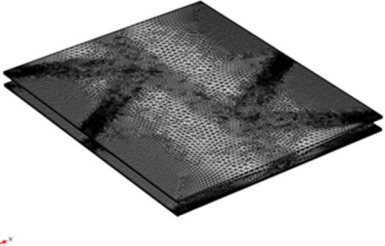
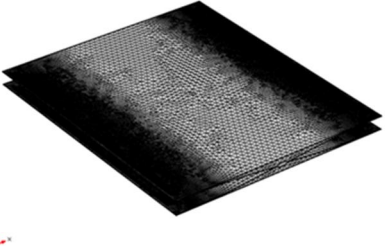
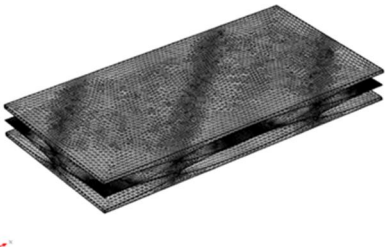
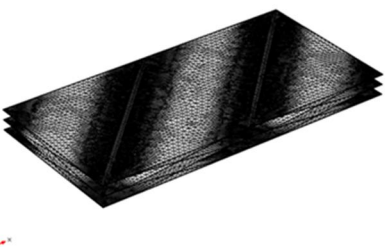
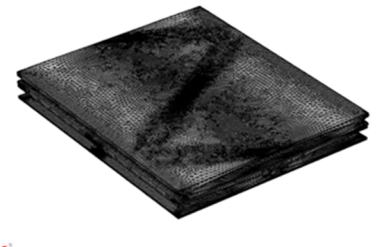
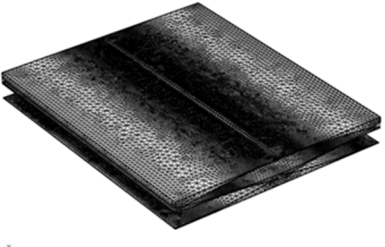
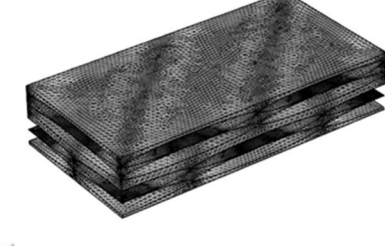
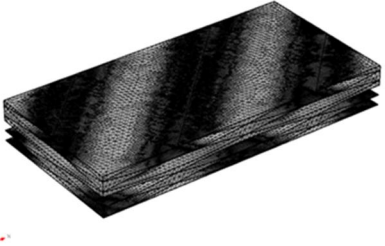
, where  $A$  is the cross-sectional area including both fluid and fiber bundles. Diagonal components of the second order permeability tensor were acquired from **Eq. (2.1.3)**.



**Figure 2.1.1.** Carbon fiber NCFs used in this study. Photographs of (a) front side and (b) back side for the NCF  $0^\circ$ . (c) Front image and (d) back image of modeled geometry for the NCF  $0^\circ$ . Photographs of (e) front side and (f) back side for the NCF  $\pm 45^\circ$ . (g) Front image and (h) back image of modeled geometry for the NCF  $\pm 45^\circ$ .

(a)	w/o shifting	Macroscale	Mesoscale for in-plane (Bundle cross-section: ellipse)	Mesoscale for out-of-plane (Bundle cross-section: lenticular)
	NCF $0^\circ$			
	NCF $\pm 45^\circ$			
(b)	w/ shifting	Macroscale	Mesoscale for in-plane (Bundle cross-section: ellipse)	Mesoscale for out-of-plane (Bundle cross-section: lenticular)
	NCF $0^\circ$			
	NCF $\pm 45^\circ$			

**Figure 2.1.2.** Geometry and 3D mesh for unit cells of the NCF  $0^\circ$  and NCF  $\pm 45^\circ$  without (a, c) and with (b, d) shifting.

(c)	w/o shifting	Mesoscale for in-plane (Bundle cross-section: ellipse)	Mesoscale for out-of-plane (Bundle cross-section: lenticular)
	NCF 0°		
	NCF ±45°		
(d)	w/ shifting	Mesoscale for in-plane (Bundle cross-section: ellipse)	Mesoscale for out-of-plane (Bundle cross-section: lenticular)
	NCF 0°		
	NCF ±45°		

**Figure 2.1.2.** Geometry and 3D mesh for unit cells of the NCF 0° and NCF ±45° without (a, c) and with (b, d) shifting.

### 2.1.3. Experimental section

Two different experiments were performed, and the measured permeability values were compared with the predicted results<sup>17-25</sup>. The radial flow test was carried out to measure the in-plane permeability of the NCF fabrics. Because it can prevent the edge effect which occurs frequently during the unidirectional experiment, more reliable data may be obtained than employing other methods. Additionally, the out-of-plane flow test was conducted to measure the out-of-plane permeability

#### 2.1.3.1. Materials

Fig. 1 shows two different types of the carbon NCFs used in this study. They were the uniaxial and biaxial fabrics. The uniaxial fabric (NCF 0°) was stitched with polyethylene yarns and stabilized with glass fibers. The biaxial fabric (NCF ±45°) was stitched only with polyethylene yarns such that the two uniaxial fabrics were bound to each other in ±45° directions. The carbon fiber was Toray T700SC12K.

Silicone oil (dimethyl siloxane polymer, DC 200F/100CS) was used as an injection resin. Because the silicone oil was a Newtonian fluid with a viscosity of  $9.7 \times 10^{-2}$  Pa·s, Darcy's law was applied to calculate the permeability.

#### 2.1.3.2. Experimental Apparatus

A transparent mold was designed and built for the measurement of the in-plane permeability as illustrated in **Fig. 2.1.3(a)**. The top and bottom plates were made of aluminum, and the top plate used to prevent the bending of the transparent plate under pressure had windows. The middle plate was made of transparent PMMA to observe the advancement of resin flow.

An additional mold for the measurement of the out-of-plane permeability was constructed as shown in **Fig. 2.1.3(b)**. The mold was made of steel and consisted of a pair

of permeable circular walls to fix fabrics.

The experimental set-up for radial flow and out-of-plane flow are illustrated schematically in **Fig. 2.1.4**. Compressed nitrogen gas was used for injection of the resin into the mold through the inlet, and the pressure transducers were used to measure pressure at each location. 5 layers of the preform were used for all the measurements.

To obtain the in-plane permeability, square preform layers with a size of 400 mm × 400 mm were placed between the middle and the bottom plates, and the fiber volume fraction was controlled by changing the space between the top and the bottom plates. Resin was injected to the in-plane mold under a pressure of 0.025 MPa, and the pressure at the inlet was measured by the pressure transducer. A digital camcorder was used to record the advancement of the resin flow front.

For the out-of-plane flow experiment, circular preform layers with a 12 cm diameter were placed between the permeable walls for uniform flow. The fiber volume fraction was also adjusted by varying the space between the two walls. Pressure was applied to the resin in the range of 0.1 ~ 0.2 MPa, and the pressures at the inlet and outlet were measured after saturation. It was assumed that the preform was fully saturated with resin when the mass flow rate became constant, and any air bubbles were not observed in the silicone oil flowing out of the mold.

### **2.1.3.3. Measurement of Permeability**

The in-plane permeabilities of the two fiber preforms, NCF 0° and NCF ±45°, were determined from unsaturated radial flow experiments at four different fiber volume fractions. The permeability of each case was calculated by using the positions of flow front, elapsed time after injection, and measured inlet pressure.

The out-of-plane permeabilities of the NCF 0° and the NCF ±45° were also measured at four different fiber volume fractions in saturated flow condition. The steady state flow rate was obtained by collecting and weighing the outflow of silicone oil during the measurement. The pressure gradient was determined using the pressure difference between the inlet and the outlet, and the permeability was calculated with Darcy's law.

#### 2.1.4. Results and discussion

**Fig. 2.1.5** shows the velocity profile and pressure field of the unit cell when the fiber volume fraction is 0.4. The fluid flow was considered in the axial, transverse, and thickness directions. The velocity profiles show that most of the resin flows through the space between the fiber bundles.

The velocity profile and pressure field were calculated numerically by considering the fabric shifting effect between the NCF layers (**Fig. 2.1.6**). Compared with the case without considering the shifting effect, the velocity profile was changed dramatically, and the average velocity decreased by a half. In particular, the out-of-plane flow of the NCF 0° showed much lower velocities.

The permeability of a preform can be calculated by using the average velocity and the pressure gradient of the unit cell. **Table 2.1.1** shows the predicted permeability at each fiber volume fraction. The permeability decreased with increase in the fiber volume fraction, and the out-of-plane permeability of the both fabrics was about 2 orders of magnitude lower than the in-plane permeability. It is shown that the permeability for the NCF 0° is lower than that for the NCF ±45° in all the directions, and the NCF 0° has more significant shifting effect than the NCF ±45°.

The flow front advancement through the NCF 0° and NCF ±45° preforms in the radial flow mold was observed with respect to time as shown in **Fig. 2.1.7(a)** and **(b)**, respectively. The elliptical flow front through the NCF 0° indicates the anisotropic property of the permeability, whereas the radially symmetric flow front through the NCF ±45° means the isotropic nature of the permeability.

To determine the in-plane permeability of the NCF 0°, the terms in the curly brackets of **Eqs. (2.1.4)** and **(2.1.5)** were plotted as a function of time for four different fiber volume fractions as shown in **Fig. 2.1.8**<sup>26</sup>. Thereafter, the in-plane permeability of each preform sample was obtained from the slope of the regression line of each graph.

$$K_1 = \{x_f^2 [2\ln(x_f/x_0) - 1] + x_0^2\} \frac{1}{t} \frac{\mu\varepsilon}{4\Delta P} \quad (2.1.4)$$

$$K_2 = \{y_f^2 [2\ln(y_f/y_0) - 1] + y_0^2\} \frac{1}{t} \frac{\mu \varepsilon}{4\Delta P} \quad (2.1.5)$$

, where  $\varepsilon$  is the porosity,  $t$  is the elapsed time after injection,  $x_f$  and  $y_f$  are the radii of the flow front,  $x_0$  and  $y_0$  are the radii of the inlet, and  $\Delta P$  is the pressure difference between the flow front and the inlet.

The in-plane permeability of the NCF  $\pm 45^\circ$  was also obtained by the same method. Due to the discontinuous resin filling of the NCF  $\pm 45^\circ$  as shown in **Fig. 2.1.7(b)**, exact observation of the flow front as a function of time was difficult. Therefore, the permeability was determined using the arrival time of the flow front at  $r_f = 17.5$  cm, where the flow front was relatively continuous and clear.

The out-of-plane permeabilities of the NCF  $0^\circ$  and the NCF  $\pm 45^\circ$  were calculated by using **Eq. (2.1.3)**<sup>27</sup> and are listed in **Table 2.1.2**. It was revealed that the in-plane and out-of-plane permeabilities of the two fabrics increased as the porosity increased. The in-plane permeability of the NCF  $\pm 45^\circ$  was slightly higher than that of the NCF  $0^\circ$ , while the out-of-plane permeability of the NCF  $\pm 45^\circ$  was much lower than that of the NCF  $0^\circ$ . This large difference in the out-of-plane permeabilities between the two fabrics could be explained by the geometric characteristics of the preforms. That is, although the carbon fibers constituting the fabrics are the same, the macro- and microscopic geometries were different. Because the NCF  $\pm 45^\circ$  consisted of two uniaxial fabrics aligned in  $\pm 45^\circ$  directions, it had more complex flow path than the NCF  $0^\circ$ . The complex flow through the NCF  $\pm 45^\circ$  resulted in relatively high flow resistance through the fabric.

In order to confirm the numerical results, the predicted permeability was compared with the measured values as shown in **Fig. 2.1.9**. Distinction between the numerical and experimental results was small in the in-plane direction, but there was a big difference in the out-of-plane permeability of the NCF  $0^\circ$  when the shift effect was not considered. Such difference decreased when the shift effect was taken into account. This occurred only in the NCF  $0^\circ$ , which mean that the NCF  $0^\circ$  was more affected by the shifting effect than the NCF  $\pm 45^\circ$ . The difference between the predicted and measured out-of-plane permeabilities could be further understood if a non-periodic stacking were considered to reflect the actual stacking geometry. However, the homogenization method is an efficient



way to predict the permeability tensor of fiber preforms with complex structure.

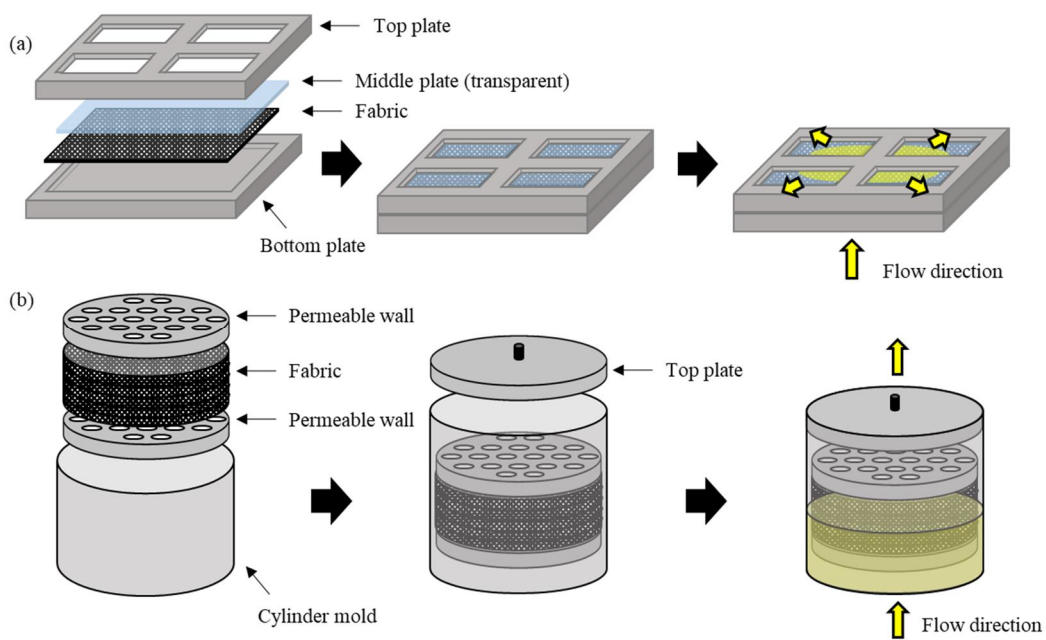


**Figure 2.1.3.** Schematic illustration of the mold used for the measurement of (a) in-plane and (b) out-of-plane permeability.

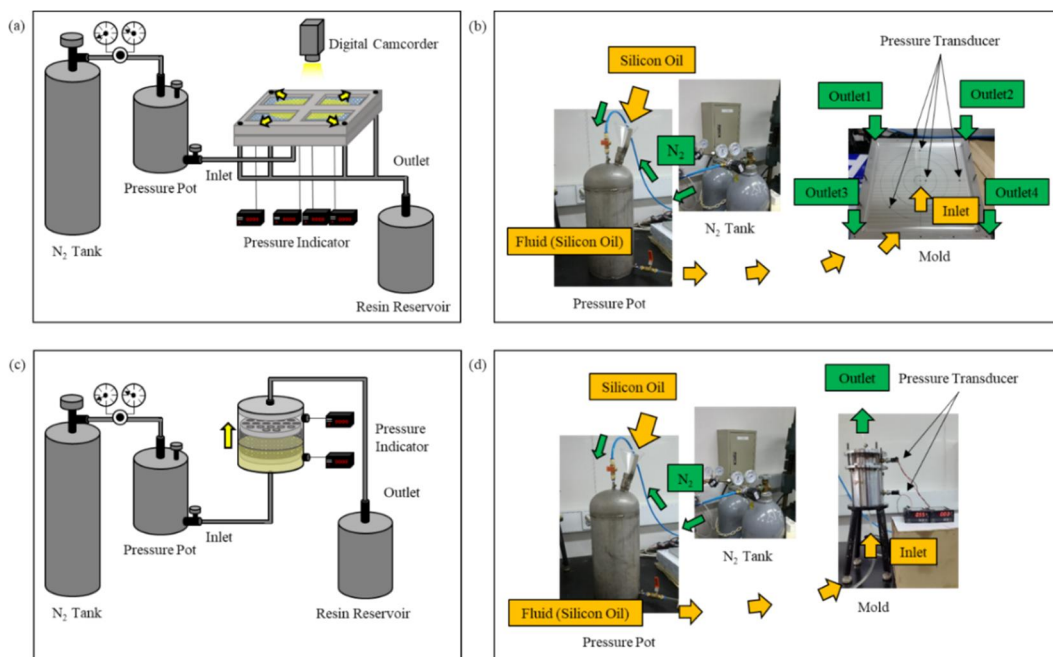


**Figure 2.1.4.** Experimental set-up for the measurement of (a, b) in-plane and (c, d) out-of-plane permeability.

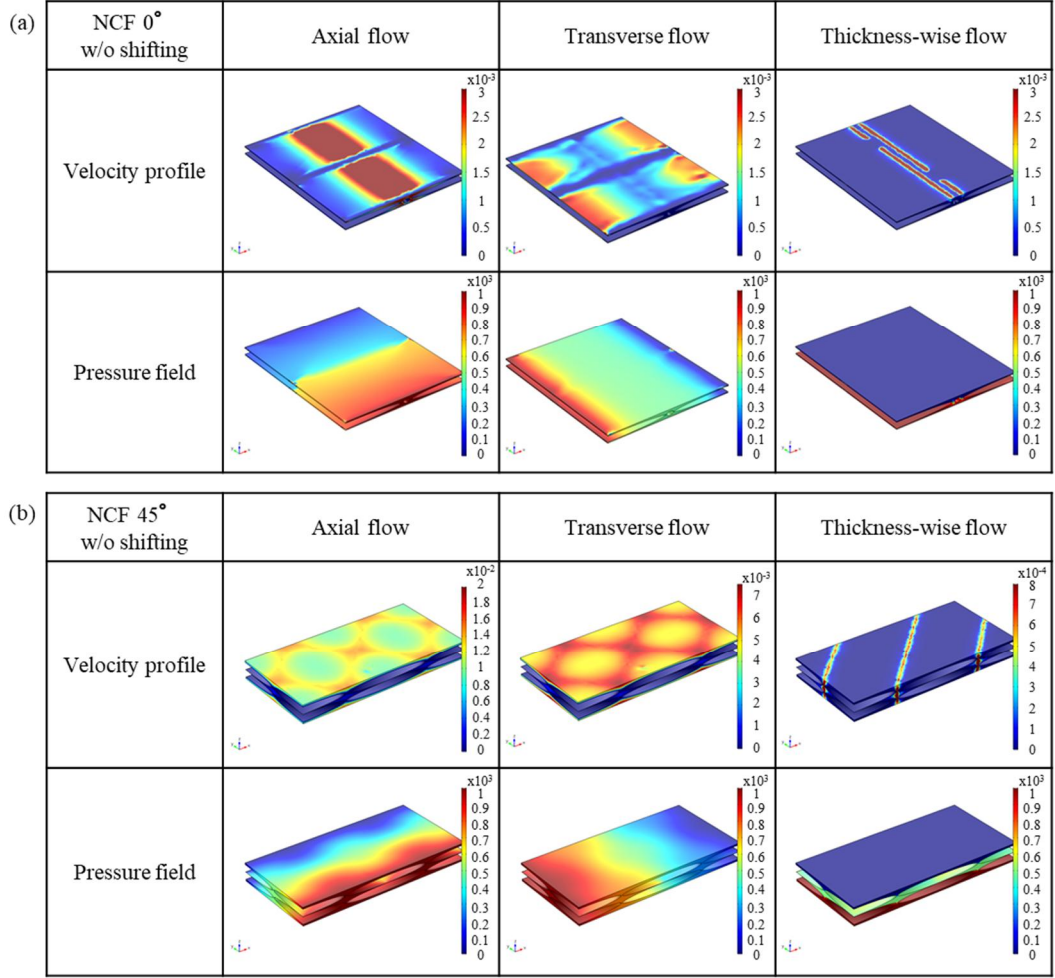


**Figure 2.1.5.** Velocity profile and pressure field without shifting effect for (a) NCF  $0^\circ$  and (b) NCF  $\pm 45^\circ$ .

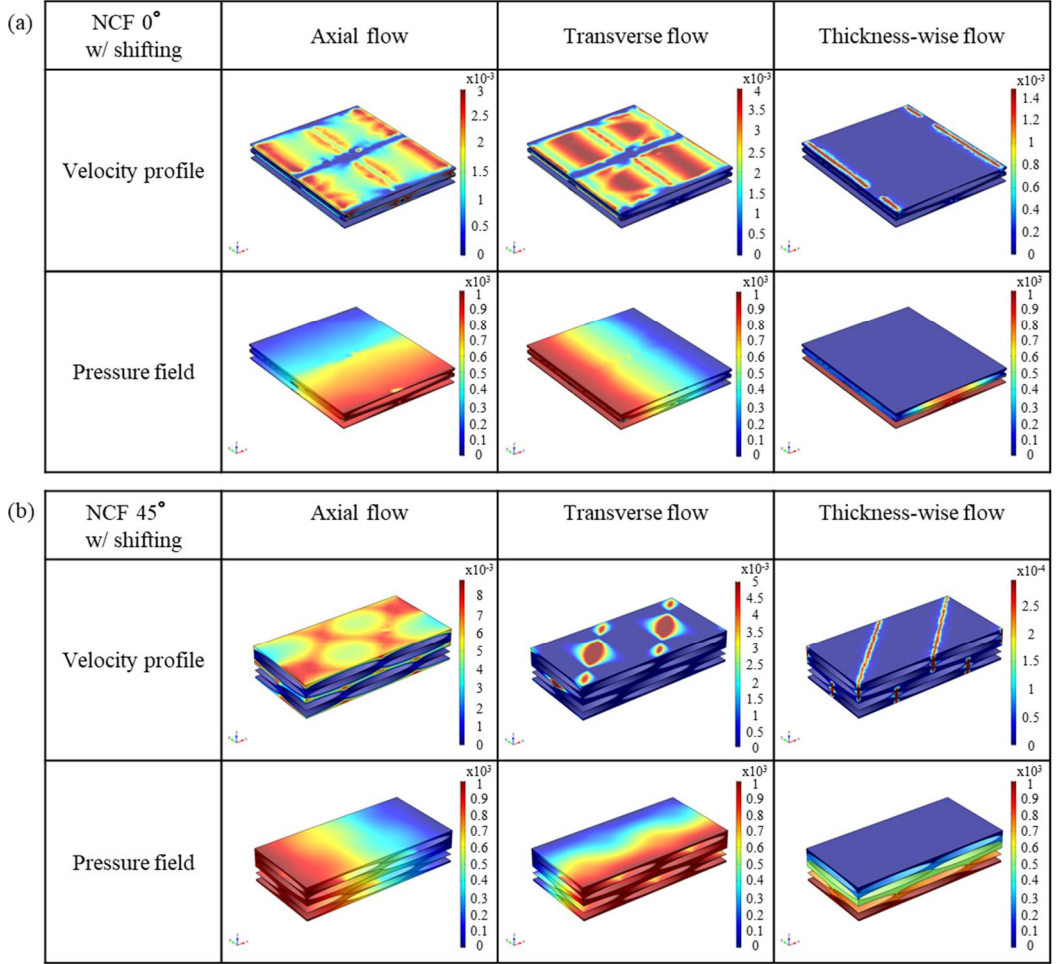


**Figure 2.1.6.** Velocity profile and pressure field with shifting effect for (a) NCF 0° and (b) NCF  $\pm 45^\circ$ .

**Table 2.1.1.** Permeability predicted for (a) NCF 0° and (b) NCF ±45°.

	NCF 0° w/o shifting			NCF ±45° w/o shifting		
Fiber volume fraction	0.448	0.491	0.588	0.418	0.477	0.589
$K_{axial} (\times 10^{-9} m^2)$	3.183	1.946	0.655	6.942	3.797	1.128
$K_{trans.} (\times 10^{-9} m^2)$	1.472	0.863	0.269			
Fiber volume fraction	0.413	0.456	0.538	0.421	0.488	0.574
$K_{thick.} (\times 10^{-12} m^2)$	89.67	36.59	13.40	2.410	0.574	0.016

	NCF 0° w/ shifting			NCF ±45° w/ shifting		
Fiber volume fraction	0.444	0.488	0.585	0.436	0.477	0.589
$K_{axial} (\times 10^{-9} m^2)$	2.096	1.419	0.496	7.116	4.153	1.170
$K_{trans.} (\times 10^{-13} m^2)$	1.871	1.230	0.471			
Fiber volume fraction	0.460	0.514	0.620	0.421	0.488	0.574
$K_{thick.} (\times 10^{-12} m^2)$	3.171	1.046	0.039	2.479	0.602	0.018

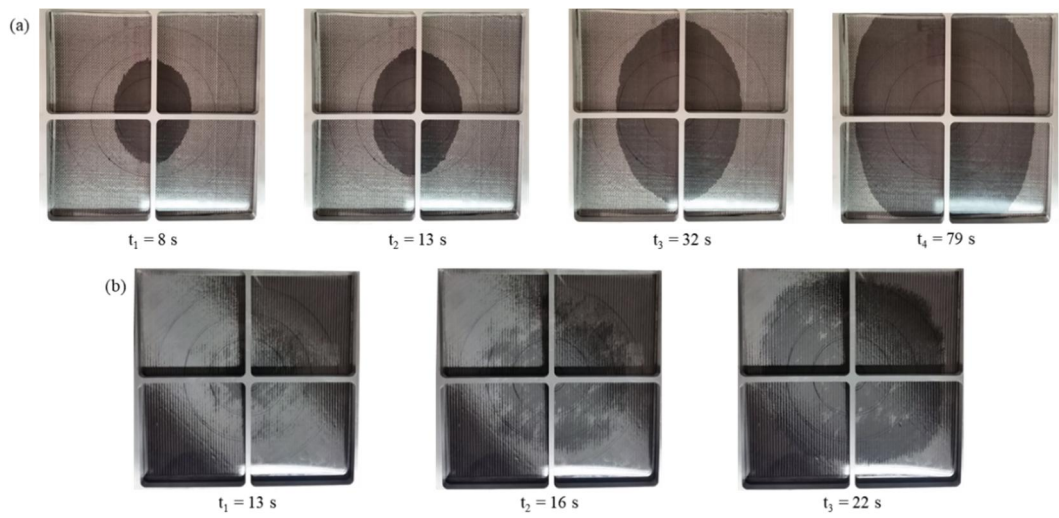


**Figure 2.1.7.** Advancement of the resin flow front for (a) NCF  $0^\circ$  (Vf = 61 %) and (b) NCF  $\pm 45^\circ$  (Vf = 69.6 %).

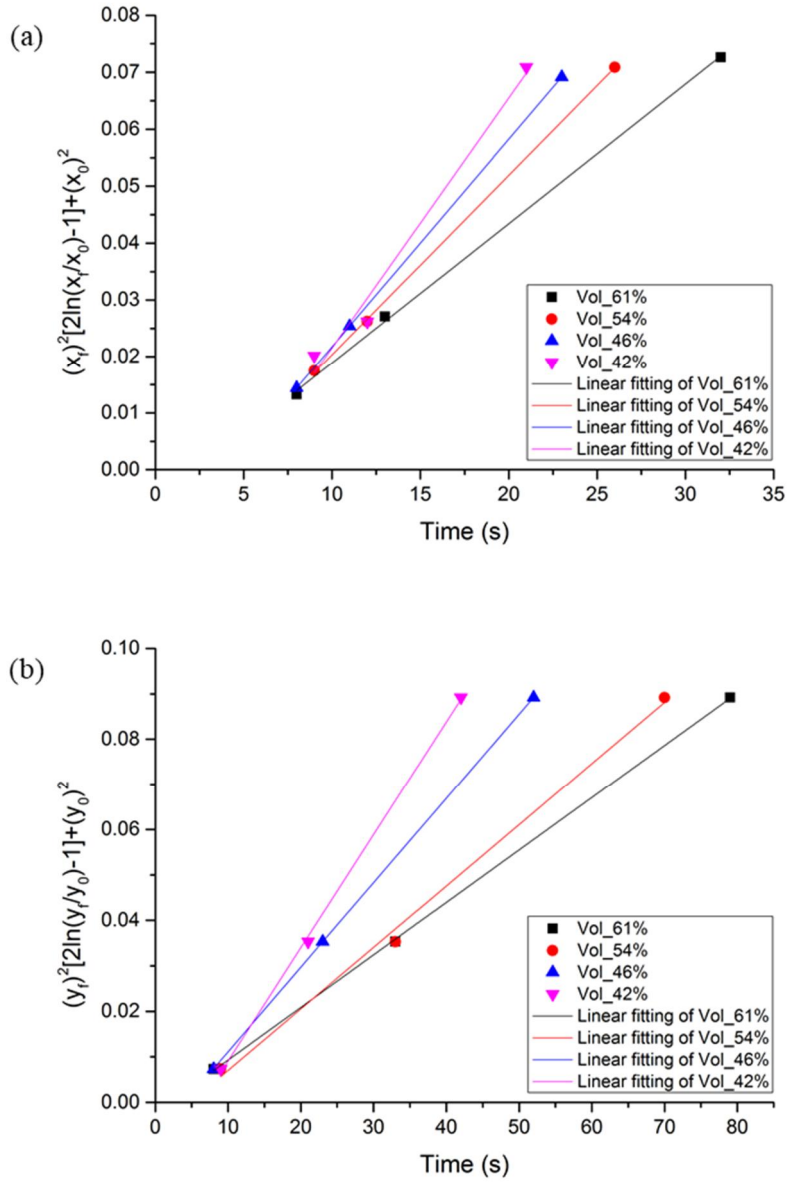


**Figure 2.1.8.** Linear fitting of the flow front for the NCF 0° in (a) the axial and (b) the transverse directions.



**Table 2.1.2.** Permeability measured for (a) NCF 0° and (b) NCF ±45°.

	NCF 0°				NCF ±45°			
Fiber volume fraction	0.416	0.457	0.538	0.610	0.425	0.488	0.574	0.696
$K_{axial} (\times 10^{-9} m^2)$	2.149	1.475	1.086	0.676	3.573	2.395	1.828	0.831
$K_{trans.} (\times 10^{-9} m^2)$	1.221	0.758	4.752	0.324				
$K_{thick.} (\times 10^{-12} m^2)$	2.011	1.174	0.499	-	0.242	0.108	0.062	-

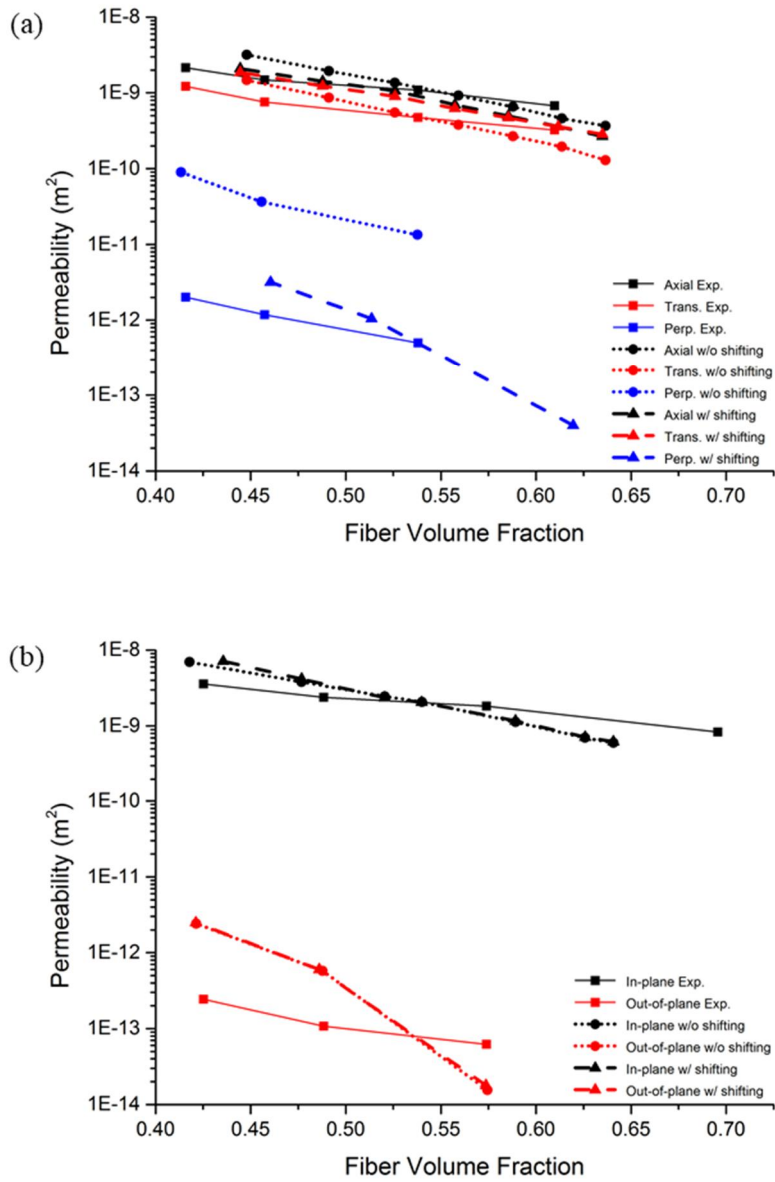


**Figure 2.1.9.** Comparison of the measured and predicted permeability of (a) NCF 0° and (b) NCF  $\pm 45^\circ$ .

### **2.1.5. Summary**

Numerical and experimental studies were carried out about the permeability of NCF fabrics. The fabric shifting effect between the NCF layers was considered in the numerical analysis. Experimental setups for the measurement of in-plane and out-of-plane permeabilities were designed and constructed. The predicted and measured in-plane permeabilities were in good agreement, but there existed a difference between the measured and predicted values of the out-of-plane permeability due to the simplified geometry of the unit cells employed in the numerical simulation. When the shifting effect was considered in the numerical modeling, the predicted permeability of the NCF  $0^\circ$  showed better agreement with the experimental result than that of the NCF  $\pm 45^\circ$ . Although robust and informative results were provided from the numerical and experimental investigations, it was also shown that more realistic unit cell structure is needed for accurate prediction.

## 2.1.6. References

1. Carman, P. C., Fluid flow through granular beds. *Trans. Inst. Chem. Eng.* **1937**, *15*, 150-166.
2. Sangani, A.; Acrivos, A., Slow flow through a periodic array of spheres. *International Journal of Multiphase Flow* **1982**, *8* (4), 343-360.
3. Gebart, B. R., Permeability of unidirectional reinforcements for RTM. *Journal of composite materials* **1992**, *26* (8), 1100-1133.
4. Nedanov, P. B.; Advani, S. G., Numerical computation of the fiber preform permeability tensor by the homogenization method. *Polymer composites* **2002**, *23* (5), 758-770.
5. Šimáček, P.; Advani, S. G., Permeability model for a woven fabric. *Polymer Composites* **1996**, *17* (6), 887-899.
6. Ngo, N.; Tamma, K., Microscale permeability predictions of porous fibrous media. *International Journal of Heat and Mass Transfer* **2001**, *44* (16), 3135-3145.
7. Song, Y.; Chung, K.; Kang, T.; Youn, J., Prediction of permeability tensor for plain woven fabric by using control volume finite element method. *Polymers & polymer composites* **2003**, *11* (6), 465-476.
8. Grössing, H.; Fauster, E.; Weninger, M.; Schledjewski, R., Influence of textile parameters on the in-plane permeability characteristics of non-crimped fabric preforms. *Polymer Composites* **2016**, *37* (6), 1854-1863.
9. Dong, S.; Liu, G.; Jia, Y.; Li, W.; Jiao, X., Study on correlation between permeability and structural parameters of non-crimped fabrics. *Journal of Composite Materials* **2016**, *50* (19), 2661-2668.
10. Karaki, M.; Hallal, A.; Younes, R.; Trochu, F.; Lafon, P., In-plane permeability prediction model for non-crimp and 3D orthogonal fabrics. *The Journal of The Textile Institute* **2018**, *109* (8), 1110-1126.
11. Rimmel, O.; Becker, D.; Mitschang, P., Maximizing the out-of-plane-permeability of preforms manufactured by dry fiber placement. *Advanced Manufacturing: Polymer & Composites Science* **2016**, *2* (3-4), 93-102.
12. Amaziane, B.; Hontans, T.; Koebbe, J., Equivalent permeability and simulation of two-phase flow in heterogeneous porous media. *Computational Geosciences* **2001**, *5* (4), 279-300.
13. Zijl, W.; Trykozko, A., Numerical homogenization of the absolute permeability using the conformal-nodal and mixed-hybrid finite element method. *Transport in Porous Media* **2001**, *44* (1), 33-62.
14. Trykozko, A.; Zijl, W.; Bossavit, A., Nodal and mixed finite elements for the numerical homogenization of 3D permeability. *Computational Geosciences* **2001**, *5* (1), 61-84.
15. Takano, N.; Zako, M.; Okazaki, T.; Terada, K., Microstructure-based evaluation of the influence of woven architecture on permeability by asymptotic homogenization theory. *Composites Science and Technology* **2002**, *62* (10-11), 1347-1356.
16. Chen, Z.; Ye, L.; Liu, H., Effective permeabilities of multilayer fabric preforms in liquid composite moulding. *Composite structures* **2004**, *66* (1-4), 351-357.
17. Adams, K. L.; Miller, B.; Rebenfeld, L., Forced in-plane flow of an epoxy resin in fibrous networks. *Polymer Engineering & Science* **1986**, *26* (20), 1434-1441.

18. Parnas, R. S.; Salem, A. J., A comparison of the unidirectional and radial in-plane flow of fluids through woven composite reinforcements. *Polymer Composites* **1993**, *14* (5), 383-394.
19. Woerdeman, D. L.; Phelan Jr, F. R.; Parnas, R. S., Interpretation of 3-D permeability measurements for RTM modeling. *Polymer Composites* **1995**, *16* (6), 470-480.
20. Lekakou, C.; Johari, M.; Norman, D.; Bader, M., Measurement techniques and effects on in-plane permeability of woven cloths in resin transfer moulding. *Composites Part A: Applied Science and Manufacturing* **1996**, *27* (5), 401-408.
21. Lai, Y. H.; Khomami, B.; Kardos, J. L., Accurate permeability characterization of preforms used in polymer matrix composite fabrication processes. *Polymer Composites* **1997**, *18* (3), 368-377.
22. Lundström, T.; Stenberg, R.; Bergström, R.; Partanen, H.; Birkeland, P., In-plane permeability measurements: a nordic round-robin study. *Composites Part A: Applied Science and Manufacturing* **2000**, *31* (1), 29-43.
23. Amico, S.; Lekakou, C., An experimental study of the permeability and capillary pressure in resin-transfer moulding. *Composites Science and Technology* **2001**, *61* (13), 1945-1959.
24. Endruweit, A.; Luthy, T.; Ermanni, P., Investigation of the influence of textile compression on the out-of-plane permeability of a bidirectional glass fiber fabric. *Polymer composites* **2002**, *23* (4), 538-554.
25. Kim, S. K.; Opperer, J. G.; Kim, D. H.; Daniel, I. M., Determination of in-plane permeability of fiber preforms by the gas flow method using pressure measurements. *Polymer composites* **2003**, *24* (1), 34-44.
26. Cho, Y. K.; Song, Y. S.; Kang, T. J.; Chung, K.; Youn, J. R., Permeability measurement of a circular braided preform for resin transfer molding. *Fibers and Polymers* **2003**, *4* (3), 135-144.
27. Chae, H. S.; Song, Y. S.; Youn, J. R., Transverse permeability measurement of a circular braided preform in liquid composite molding. *Korea-Australia Rheology Journal* **2007**, *19* (1), 17-25.

## 2.2. Numerical simulation and processing

### 2.2.1. Introduction

In recent years, many studies have focused on improving fuel efficiency by using lightweight components in automotive industry. Indeed, weight reduction becomes an important issue due to high oil prices and strict fuel efficiency regulations. This can be achieved through several approaches: new structural design, processing, and materials. In particular, replacing existing heavy materials with lightweight materials can induce a big impact. However, the application of such composite materials to automotive parts are still limited due to their long processing cycle time and production cost.

Carbon fiber reinforced plastics (CFRPs) used in automobile are mostly manufactured using the resin transfer molding (RTM) process, which can fabricate complex structure and thick product <sup>1-4</sup>. However, since various problems occur during manufacturing large and complex parts, numerical simulation of RTM can help design and optimize the process. In general, the simulation focuses on the filling step providing a guide regarding the processing conditions such as flow rate and pressure <sup>5</sup>. For example, by predicting the resin flow behavior, it can be determined whether or not a fiber preform is completely filled. In addition, the resin inlet and vent positions can be optimized based on the simulation result <sup>6, 7</sup>. Since a number of products manufactured via RTM are simple and thin, it has been assumed that the flow in the thickness direction is neglected in the simulation <sup>8-15</sup>. However, it is necessary to carry out three dimensional flow analysis to comprehend underlying physics regarding flow behavior in complex and thick parts produced using RTM <sup>16-23</sup>.

In this study, numerical and experimental studies have been carried out to manufacture a large and complex CFRP part. As a representative part to substitute metallic parts, an automotive wheel rim was selected and fabricated (**Fig. 2.2.1**). The wheel rim is a component that can play an important role in reducing the weight of automobiles. 3D numerical simulation was conducted to investigate the resin flow behavior in the complex mold.

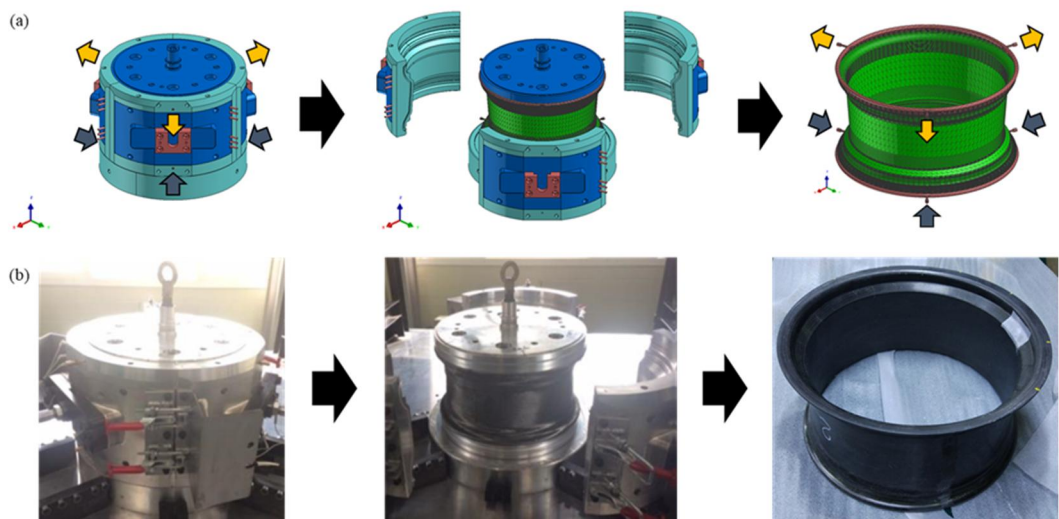


**Figure 2.2.1.** (a) Schematic illustration and (b) photographs of the mold and the CFRP.

## 2.2.2. Numerical analysis

### 2.2.2.1. Governing equation

Numerical analysis of RTM was carried out using finite element method. The filling process was simulated at constant temperature assuming that the resin was an incompressible and Newtonian fluid. Fiber preform generally has anisotropic permeability values depending on the fiber orientation. For a thin CFRP, the flow in the thickness direction is negligible compared with those in the other directions. Therefore, the permeability is considered as a 2D tensor. However, the out-of-plane permeability needs to be considered to manufacture thick composite parts since the flow in the thickness direction is meaningful. As a result, 3D modeling can provide more improved accuracy and reliability of results than 2D modeling. When the resin is incompressible fluid, pressure and velocity fields are obtained by solving the following equations: Darcy's law (Eq. 2.2.1) and continuity equation (Eq. 2.2.2).

$$\mathbf{u} = \frac{\mathbf{K}}{\mu} \cdot \nabla P \quad (2.2.1)$$

$$\nabla \cdot \mathbf{u} = 0 \quad (2.2.2)$$

, where  $\mathbf{u}$  is the velocity vector of fluid,  $\mathbf{K}$  is the permeability tensor of porous medium,  $\mu$  is the Newtonian viscosity of fluid, and  $\nabla P$  is the pressure gradient vector.

Darcy's law can be integrated into continuity equation for incompressible fluid to obtain the pressure field as follows:

$$\nabla \cdot \left( \frac{\mathbf{K}}{\mu} \cdot \nabla P \right) = 0 \quad (2.2.3)$$

A fill factor  $f$  is introduced to track the evolution of the flow front:

$$\frac{\partial f}{\partial t} + \nabla \cdot (\mathbf{u}f) = 0 \quad (2.2.4)$$

, where  $0 \leq f < 1$  is defined as unsaturated region, so the pressure is  $p = 0$ .  $f = 1$  is defined as saturated region and the pressure is  $p \geq 0$ .



The macro/micro-void formation is related to the flow velocity and flow front of resin. At low flow velocity, macro-voids tend to be generated, whereas high flow velocity leads to micro-void formation. The formation of the macro- (Eq. 2.2.5) and micro-voids (Eq. 2.2.6) can be modeled as follows<sup>24, 25</sup>:

$$-1574 \cdot v + 12.82 \quad (2.2.5)$$

$$100.5 \cdot v + 1.27 \quad (2.2.6)$$

, where  $v$  is the component of the velocity vector.

In order to obtain more accurate void contents, it is preferable to conduct an experiment with same resin viscosity in advance to determine the equation. However, in this study, it is focused on whether improvements have been made between several cases rather than predicting the exact void contents value.

#### 2.2.2.2. Geometric modeling

The geometrical structure of the CFRP wheel rim is shown in Fig. 2.2.2. The 3D model consisted of the preform parts (i.e., the green and blue regions) and the distribution media part (i.e., the Brown region). The preform parts were occupied by two different non-crimp fabrics, NCF 0° and NCF ±45° (Fig. 2.2.3). The NCF 0° had a low permeability and was placed inside the rim. The NCF ±45° with a high permeability was located outside the rim. On the other hand, since the NCF 0° had stronger anisotropic feature than the NCF ±45°, it was stacked in the circumferential direction to further reinforce the mechanical properties in that direction. For the simulation, the mesh consisted of about 1.28 million tetrahedral elements and was built more finely in the complex region.

#### 2.2.2.3. Materials and processing conditions

Epoxy resin ( $\rho = 1145 \text{ kg/m}^3$ ,  $\mu = 0.5 \text{ Pa} \cdot \text{s}$ ) was used as a liquid resin. The used carbon fiber ( $\rho = 1800 \text{ kg/m}^3$ ) was supplied by Toray® T700SC12K. The permeability tensor of each fabric was measured from our previous study as listed in **Table 2.2.1**.

The permeability and fiber volume fraction values were assigned to the elements. The distribution media was given a permeability of  $10^{-7}$  in all the directions. To deal with the orientation of the fiber preform, the local coordinate systems were employed: circumferential, axial, and radial axes (**Fig. 2.2.4**).

A constant inlet pressure of 2 bar was imposed. This value coincided with the experimental one. The inlet gates and outlet vents were marked by the navy and yellow arrows, respectively as presented in **Fig. 2.2.1a**.

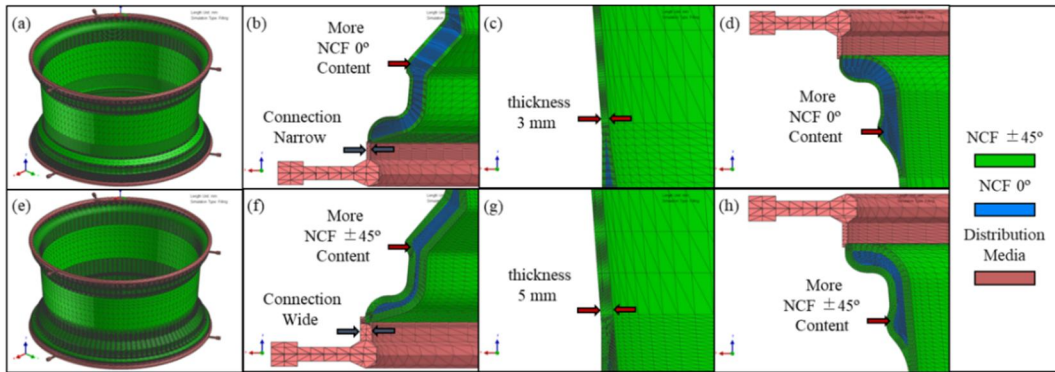


**Figure 2.2.2.** Overall geometry and magnified cross-section of the CFRP rim: (a~d) for Case 1 and (e~h) for Case 4.

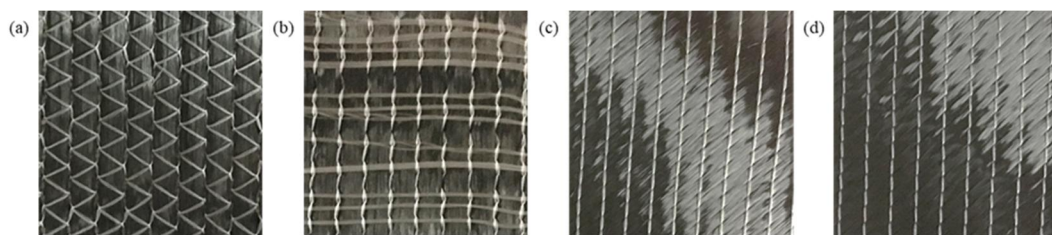


**Figure 2.2.3.** Photographs of the NCF used in this study. (a) Front side and (b) back side for the NCF  $0^\circ$ . (c) Front side and (d) back side for the NCF  $\pm 45^\circ$ .

**Table 2.2.1.** Fiber volume fraction and permeability of the NCFs used in this study.

	NCF 0°	NCF ±45°
Fiber volume fraction	0.416	0.425
$K_{axial} (\times 10^{-9} m^2)$	2.149	3.573
$K_{trans.} (\times 10^{-9} m^2)$	1.221	
$K_{thick.} (\times 10^{-12} m^2)$	2.011	0.242

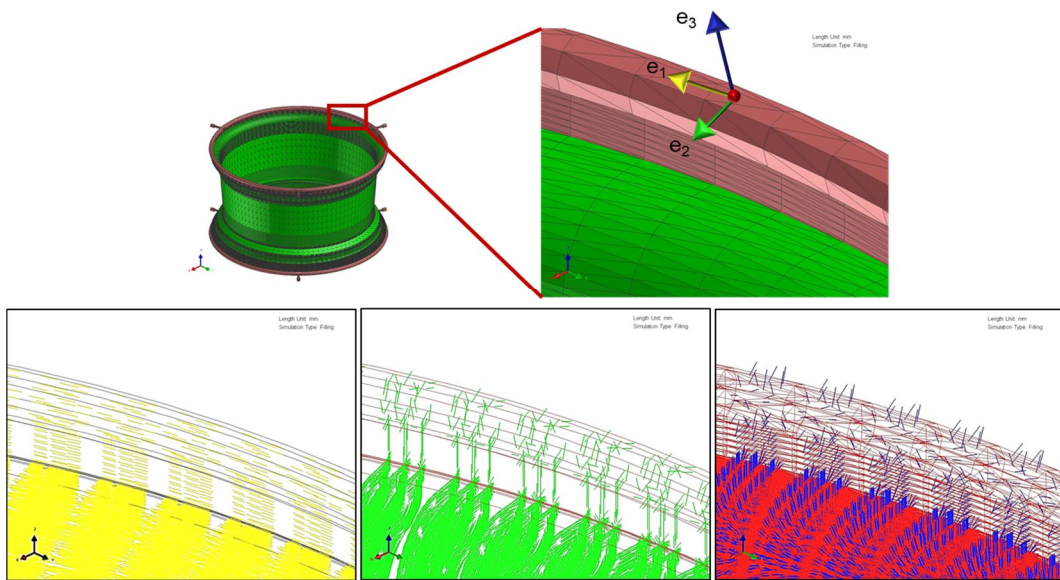


**Figure 2.2.4.** Local and global coordinates:  $e_1$ ,  $e_2$ , and  $e_3$  indicate axial, transverse, and thickness directions in the local coordinate, respectively.

### **2.2.3. Experimental section**

Based on the results of numerical simulation, the mold geometry and preform structure were upgraded. Considering Cases 1 and 4, two wheel rims were fabricated experimentally. Micro-CT measurement was carried out to observe the voids inside the manufactured products<sup>26, 27</sup>. A X-ray Micro-CT system (Skyscan 1172) was employed with 59 kV and 10 Mp X-ray source. The micro-CT system was used to perform 2D image analysis and realistic 3D visualization.

#### 2.2.4. Results and discussion

The numerical simulation was carried out to predict the resin flow behavior and the void content. Based on these results, the mold was designed, and the preforms were laminated. For the simulation, the following cases were considered:

Case 1: Narrow connection between the distribution medium and the thin preform.

Case 2: Wide connection between the distribution medium and the thin preform.

Case 3: Narrow connection between the distribution medium and the thick preform.

Case 4: Wide connection between the distribution medium and the thick preform.

The macro-void content is displayed in **Fig. 2.2.5**. Compared with Case 1, Case 2 showed the improved resin flow behavior such as the reduced filling time by means of widening the connection part. However, Case 3, which employed relatively thick preform and high content of NCF  $\pm 45^\circ$  with high permeability, showed the poor resin flow behavior such as the increased filling time. This indicates that the inlet geometry played a major role in determining the resin flow behavior in the filling stage. More detailed comparison was made between Case 1 and Case 4.

**Fig. 2.2.6** shows the flow front of resin at the given filling time for Case 1 and Case 4. The resin impregnated the distribution medium in several seconds and then flowed evenly along the z direction in both cases. The predicted total filling times were about 1091.1 s for Case 1 and 775.0 s for Case 4, respectively. Case 4 had a larger volume of the distribution medium than Case 1 because Case 1 employed the wide connection between the distribution medium and the preform. Therefore, Case 4 needed more time to fill the distribution medium at the beginning of filling stage than Case 1. However, the entire filling stage of Case 4 was facilitated more rapidly by the wide connection (**Fig. 2.2.7**).

**Fig. 2.2.8** shows the results of the macro-voids predicted numerically. Case 4 was found to have the significantly reduced void content compared to Case 1. As demonstrated above, several differences between these two cases existed: the thickness of the connection part, the preform thickness and the fabric layer structure. Hence, in order to minimize the void content not only the inlet geometry but also the fabric structure need to be controlled properly.



As shown in **Fig. 2.2.9**, Case 4 had much lower void content than Case 1. Since one pixel size of the figure set as 11.55  $\mu\text{m}$ , **Fig. 2.2.9** shows all voids (including macro- and micro- voids) of a size larger than 11.55  $\mu\text{m}$ . As it is difficult to distinguish macro-voids from micro- voids accurately, higher resolution was set and the micro-CT experiments were performed again. The shape of the fiber bundle can be confirmed, but the distinguishment between macro- and micro-voids is still difficult at high resolution. Also, this study focused whether improvements have been made in several cases rather than distinguishing macro-voids from micro-voids. So, the experiments were conducted at normal resolution. The results indicate that numerical simulation is an efficient tool to optimize real manufacturing processes. In addition, the weight of the developed CFRP wheel is 10.5kg, which is 25% lighter than conventional aluminum wheels with the same size. This suggests that CFRP composites are sufficiently applicable to the automotive wheels.

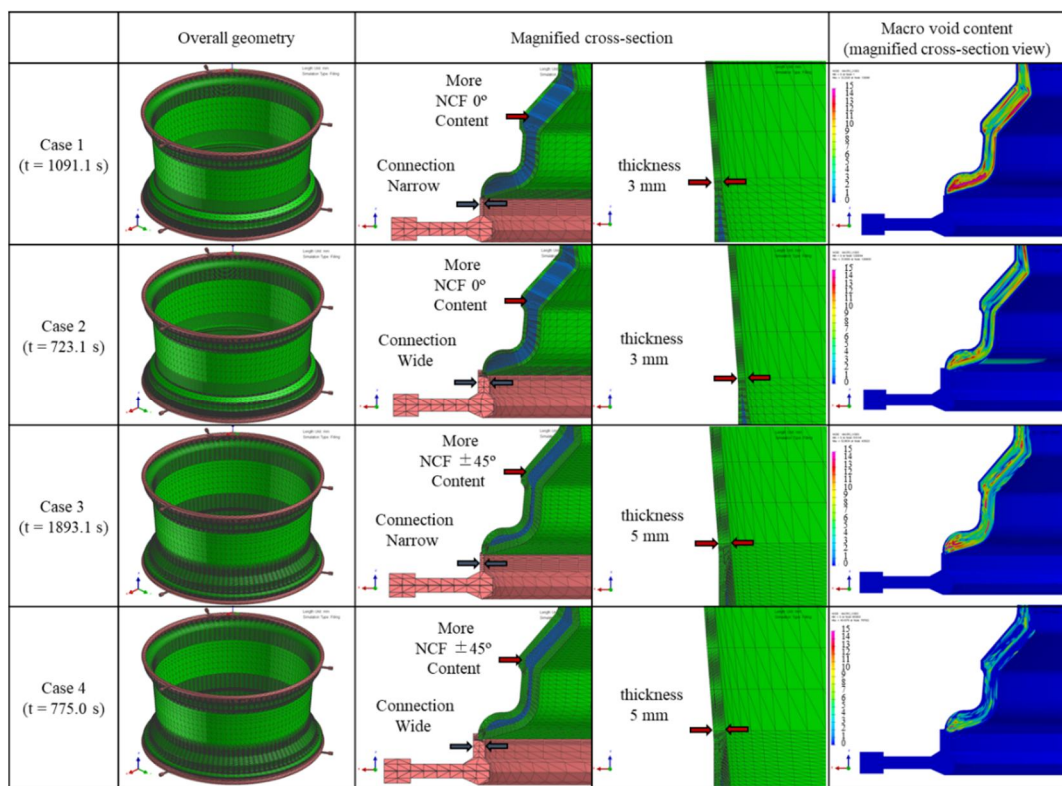


**Figure 2.2.5.** Geometry and macro-void content of the CFRP rims.

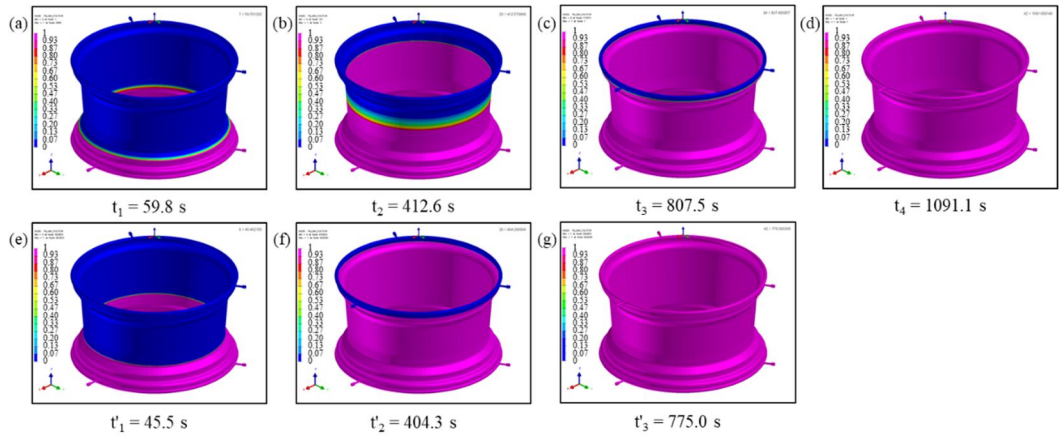


**Figure 2.2.6.** Numerical results of the flow front: (a~d) for Case 1 and (e~g) for Case 4.

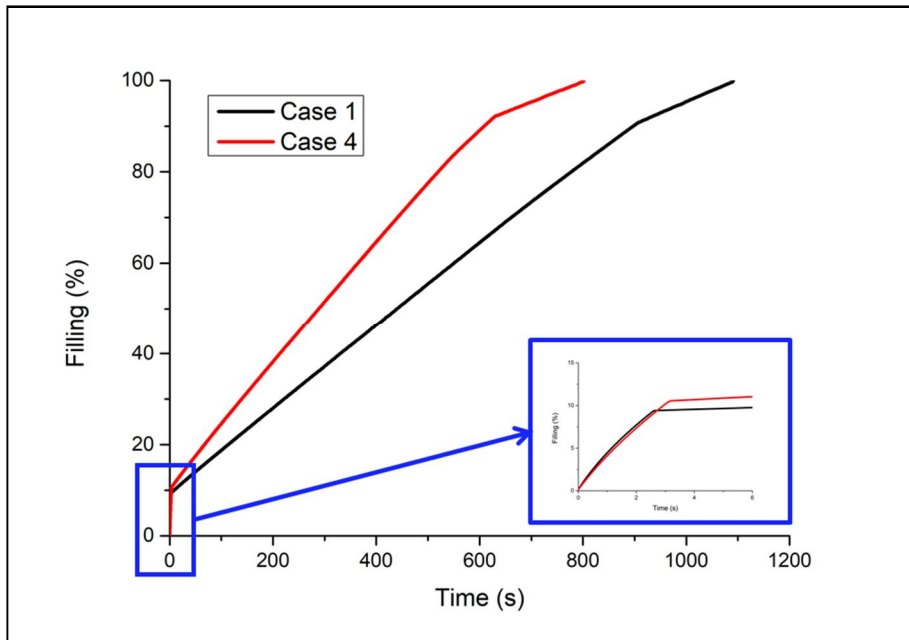


**Figure 2.2.7.** Filling percentage as a function of the time.

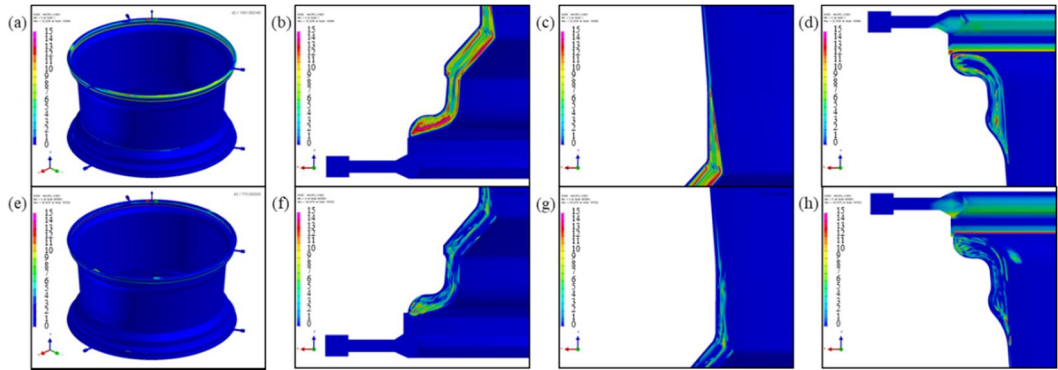


**Figure 2.2.8.** Overall and magnified cross-sectional views of the macro-void content calculated numerically: (a~d) for Case 1 and (e~h) for Case 4.

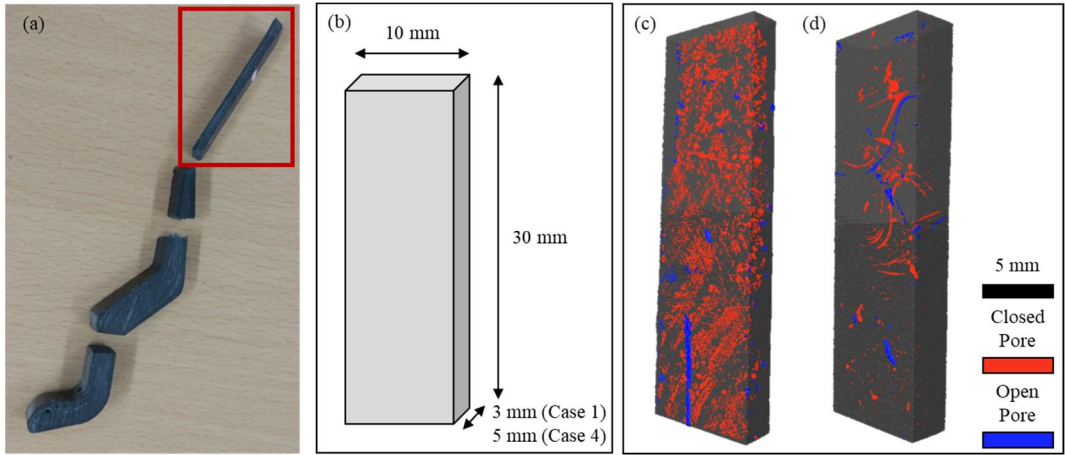


**Figure 2.2.9.** (a) Photograph of the sectioned parts from the produced wheel rim. (b) Dimensional details of the specimen for Micro-CT. Images of voids in the wheel rim: (b) for Case 1 and (c) for Case 4.

### **2.2.5. Summary**

The 3D numerical analysis was performed to investigate the resin flow behavior during the RTM process. To improve the flow behavior and minimize the void formation, the mold geometry and the fabric structure were analyzed numerically. Based on the optimized numerical results, the automotive wheel rims were manufactured. The voids inside the manufactured CFRP wheels were measured by the micro-CT equipment. It was found that the numerical and experimental results were in good agreement with each other, and the numerical optimization led to significant improvement in the quality of the product.

## 2.2.6. References

1. Bruschke, M.; Advani, S. G., A finite element/control volume approach to mold filling in anisotropic porous media. *Polymer composites* **1990**, *11* (6), 398-405.
2. Young, W.; Fong, K. H. L.; Lee, L. J., Flow simulation in molds with preplaced fiber mats. *Polymer composites* **1991**, *12* (6), 391-403.
3. Young, W. B., Three-dimensional nonisothermal mold filling simulations in resin transfer molding. *Polymer Composites* **1994**, *15* (2), 118-127.
4. Laurenzi, S.; Grilli, A.; Pinna, M.; De Nicola, F.; Cattaneo, G.; Marchetti, M., Process simulation for a large composite aeronautic beam by resin transfer molding. *Composites Part B: Engineering* **2014**, *57*, 47-55.
5. Young, W. a.; Rupel, K.; Han, K.; Lee, L. J.; Liou, M. J., Analysis of resin injection molding in molds with preplaced fiber mats. II: Numerical simulation and experiments of mold filling. *Polymer composites* **1991**, *12* (1), 30-38.
6. Young, W.-B., Gate location optimization in liquid composite molding using genetic algorithms. *Journal of Composite Materials* **1994**, *28* (12), 1098-1113.
7. Kim, B. Y.; Nam, G. J.; Ryu, H. S.; Lee, J. W., Optimization of filling process in RTM using genetic algorithm. *Korea-Australia Rheology Journal* **2000**, *12* (1), 83-92.
8. Chan, A.; Hwang, S. T., Mold-filling simulations for the injection molding of continuous fiber-reinforced polymer. *Polymer Engineering & Science* **1988**, *28* (5), 333-339.
9. Chan, A. W.; Hwang, S. T., Modeling of the impregnation process during resin transfer molding. *Polymer Engineering & Science* **1991**, *31* (15), 1149-1156.
10. Coulter, J. P.; Guceri, S. I., Resin impregnation during the manufacturing of composite materials subject to prescribed injection rate. *Journal of Reinforced Plastics and Composites* **1988**, *7* (3), 200-219.
11. Li, S.; Gauvin, R., Numerical analysis of the resin flow in resin transfer molding. *Journal of Reinforced Plastics and Composites* **1991**, *10* (3), 314-327.
12. Chan, A. W.; Hwang, S. T., Modeling nonisothermal impregnation of fibrous media with reactive polymer resin. *Polymer Engineering & Science* **1992**, *32* (5), 310-318.
13. Lin, R.; Lee, L. J.; Liou, M. J., Mold filling and curing analysis in liquid composite molding. *Polymer Composites* **1993**, *14* (1), 71-81.
14. Yoo, Y. E.; Lee, W. I., Numerical simulation of the resin transfer mold filling process using the boundary element method. *Polymer Composites* **1996**, *17* (3), 368-374.
15. Hattabi, M.; Echaabi, J.; Bensalah, M. O., Numerical and experimental analysis of the resin transfer molding process. *Korea-Australia Rheology Journal* **2008**, *20* (1), 7-14.
16. Trochu, F.; Gauvin, R.; Gao, D. M., Numerical analysis of the resin transfer molding process by the finite element method. *Advances in Polymer Technology: Journal of the Polymer Processing Institute* **1993**, *12* (4), 329-342.
17. Bruschke, M.; Advani, S., A numerical approach to model non-isothermal viscous flow through fibrous media with free surfaces. *International Journal for numerical methods in fluids* **1994**, *19* (7), 575-603.
18. Lee, L. J.; Young, W.; Lin, R., Mold filling and cure modeling of RTM and SRIM processes. *Composite structures* **1994**, *27* (1-2), 109-120.



19. Shojaei, A.; Ghaffarian, S. R.; Karimian, S. M.-H., Modeling and simulation approaches in the resin transfer molding process: a review. *Polymer Composites* **2003**, 24 (4), 525-544.
20. Isoldi, L. A.; Oliveira, C. P.; Rocha, L. A.; Souza, J. A.; Amico, S. C., Three-dimensional numerical modeling of RTM and LRTM processes. *Journal of the Brazilian Society of Mechanical Sciences and Engineering* **2012**, 34 (2), 105-111.
21. Poodts, E.; Minak, G.; Mazzocchetti, L.; Giorgini, L., Fabrication, process simulation and testing of a thick CFRP component using the RTM process. *Composites Part B: Engineering* **2014**, 56, 673-680.
22. Oliveira, I. R. d.; Amico, S. C.; Souza, J. A.; de Lima, A. G. B. In *Numerical analysis of the resin transfer molding process via PAM-RTM software*, Defect and Diffusion Forum, Trans Tech Publ: 2015; pp 88-93.
23. García-Manrique, J. A.; Hoto, R.; Gascón, L.; Andrés, J., A numerical simulation of woven/anionic polyamide 6 composite part manufacturing using structural reactive injection moulding process. *Journal of Thermoplastic Composite Materials* **2016**, 29 (2), 219-233.
24. Patel, N.; Rohatgi, V.; Lee, L. J., Micro scale flow behavior and void formation mechanism during impregnation through a unidirectional stitched fiberglass mat. *Polymer Engineering & Science* **1995**, 35 (10), 837-851.
25. Ruiz, E.; Achim, V.; Soukane, S.; Trochu, F.; Bréard, J., Optimization of injection flow rate to minimize micro/macro-voids formation in resin transfer molded composites. *Composites science and technology* **2006**, 66 (3-4), 475-486.
26. Lee, D. J.; Oh, H.; Song, Y. S.; Youn, J. R., Analysis of effective elastic modulus for multiphased hybrid composites. *Composites Science and Technology* **2012**, 72 (2), 278-283.
27. Hwang, S. H.; Lee, D. J.; Youn, H. R.; Song, Y. S.; Youn, J. R., Effects of fiber length distribution on flow property and internal microstructure of an injection molded part. *Macromolecular Research* **2015**, 23 (9), 844-849.

## **2.3. Product properties measurements**

### **2.3.1. Introduction**

Measurements of product properties are an important indicator for evaluating a product and it can be seen how material's original properties are implemented in the process of manufacturing the product. The various material properties and analysis methods mostly include mechanical, electrical, optical and thermal properties. In this study, mechanical and thermal properties, as well as viscoelastic behavior and structural confirmation through micro-CT were carried out.

Mechanical properties mean resistance to deformation and fracture of the material by external forces. In other words, it is expressed by the relation of deformation to the stress externally applied. In this relationship, values such as elastic modulus, tensile strength, compressive strength, bending strength, elongation, fatigue strength and hardness can be obtained <sup>1-5</sup>.

In many cases, the mechanical properties depend on the temperature at which the material is used or the temperature at which the material is received during processing. Understanding the thermal properties of a material helps in understanding the mechanical damage of the materials with varying temperatures or in selecting materials with fast heat transfer. In relation to thermal properties, the characteristics of thermal capacity, thermal expansion, and thermal conductivity can be found. Thermal expansion is the result of thermal energy that changes the dimension of the material. Thermal conductivity represents the rate at which heat is transferred to the material. It is affected by the type and defects of the material and the temperature <sup>6, 7</sup>.

The dynamic viscoelastic analysis is to measure the stress-strain relationship of the specimen by periodic deformation. The principle of dynamic viscoelasticity measurement is based on the viscoelastic properties of polymers. Viscoelasticity means that a material has both viscosity and elasticity, and when external energy is applied to a material, the energy is converted into heat energy by the viscosity, stored and released by the elasticity. In a particular polymer, the relative ratio of consumed and stored-released energy depends on the nature of the external deformation, especially the frequency. The energy loss

shows the maximum value around the glass transition temperature, which is the starting point of full-scale molecular motion. Based on this, the glass transition temperature is determined<sup>8-12</sup>.

High-resolution computerized tomography (micro-CT) provides an increasingly practical solution to the measurement of the internal fiber distribution, as computer technology continues to evolve. Using X-radiation as a transmission probe, this technology affords detailed microstructural information from almost any material. This technique, which is a non-destructive test (NDT) method, also eliminates sample preparation and associated artifacts. Moreover, micro-CT data can be readily presented in one-, two- and three-dimensional formats, suitable for observation and measurement for a variety of purposes.

### 2.3.2. Experimental section

The thermal, mechanical, viscoelastic and structural characteristics of the developed products (Developed Rim, DR) were evaluated. It was compared with benchmark product (Benchmark Rim, BM) to verify product reliability. All specimens used flat parts of the product, ie six NCF  $\pm 45^\circ$  fabrics are laminated.

Specific heat and thermal conductivity were measured to evaluate the thermal properties of the developed product. The specimens were made to fit the pan for the measurement equipment. Specific heat was measured by Differential Scanning Calorimeter (DSC). The test conditions were as follows: the temperature range was from -10 to 150 °C, and the heating rate was 20 °C/min.

Since the carbon fiber composite material has a low thermal conductivity value, a thermal conductivity meter (Laser Flash Analysis, LFA) with a wide temperature range and thermal conductivity range was selected as the thermal conductivity measurement method. The LFA measurement, which is a noncontact measurement method, calculates thermal conductivity by measuring the heat delivered by a laser fired from a laser light source over time to the opposite side of the specimen after heating one side of the specimen. The specimen is made of a coin with a diameter of 1 cm. The test conditions were as follows: the temperature was room temperature and the measured direction was the thickness direction of specimen.

The elastic modulus and tensile strength measurements were carried out using Universal Testing Machine (UTM). Specimens were produced according to ASTM D3039 standard. The specimen size is 110 mm (L)  $\times$  20 mm (W) in coupon form. In order to prevent the slip phenomenon between the jig and the specimen during the tensile test, the epoxy fiber-impregnated tab was attached to the glass fiber with epoxy adhesive. The test conditions were as follows: the tensile speed is 2 mm / min and the gauge length is 60 mm.

The storage and loss modulus measurements were performed using Dynamic Mechanical Analysis (DMA). The method of measurement was a compression method and the specimen was made in a coin with a diameter of 1 cm. The test conditions were as follows: the oscillatory force is 10 N, displacement is 10  $\mu$ m, frequency is 1 Hz, the

temperature range was from 25 to 200 °C and the heating rate was 3 °C/min.

Micro-CT measurements were performed to confirm the three-dimensional structure. An X-ray Micro-CT system (Skyscan 1172) was employed with 59 kV and 10 Mp X-ray source. DR specimens were 3 cm in length and 1 cm in width. BM specimens were 3 cm long and 0.5 cm wide.

### 2.3.3. Results and discussion

The specific heat was obtained from the heat flow value according to the temperature as shown in **Fig. 2.3.1**. As a result, the specific heat gradually increased. Both products had a value of about 1 J/g·°C at room temperature. In addition,  $T_g$  can be measured by DSC, but  $T_g$  of thermosetting polymer is generally difficult to confirm. In the case of developed product (DR), it was difficult to confirm the  $T_g$  because epoxy resin was used which is a thermosetting polymer. In the benchmark product (BM), there is no information on the resin, so it is impossible to confirm. But it was predicted that the thermosetting resin was used because it was difficult to confirm the  $T_g$  as shown in **Fig. 2.3.1**.

The thermal conductivity measurement results showed that both samples had low thermal conductivity values similar to those of typical carbon composites (0.1 ~ 0.4 W/m·K). At room temperature, the DR specimen has a value of 0.18 W/m·K, and the benchmark specimen has a value of 0.20 W/m·K. The yellow background in the **Fig. 2.3.2** shows the range of thermal conductivity values of typical carbon fiber composites.

**Fig. 2.3.3** shows the stress-strain curve (s-s curve) after three tensile tests, showing a relatively low deviation between specimens. The elastic modulus is calculated in the elongation range of 0.05 to 0.25%, and the elastic modulus of DR and BM specimen are 4984 MPa and 2975 MPa, respectively. The s-s curve shows a tensile strength of 171.4 MPa when the elongation of the DR specimen is 22.6%. The BM specimen has a tensile strength of 148.0 MPa when the elongation is 18.24%. Compared with the results of BM specimens, the elastic modulus of the DR specimen was 68%, the tensile strength was 16%, and the elongation rate was 24% higher.

The DMA results (**Fig. 2.3.4 (a)**) show that the storage modulus of the DR at high temperature is stable and the loss modulus is reduced. As the heat generated during vehicle driving and stopping is transferred to the wheel, the change in elasticity at high temperatures of composite materials is important, and the DR has been shown to have stable properties at high temperatures. The results of tangent delta (**Fig. 2.3.4 (b)**) defines  $T_g$  as the temperature corresponding to peak on the graph, with storage elasticity divided by loss elasticity. DR specimen has a max. storage modulus of 259 MPa at 81 °C and a max. loss modulus of 63 MPa at 83 °C. And  $T_g$  is about 80 to 95 °C. On the other hand,

the BR specimen has a max. storage modulus of 64 MPa at 119 °C and a max. loss modulus of 8 MPa at 126 °C. Tg is about 62 °C and 123 °C.

The results for the micro-CT measurement are as shown in **Fig. 2.3.5** and **Table. 2.3.1**. Closed porosity is the lowest for BM specimen at 0.15%, but the total porosity is 0.21%. On the other hand, the total porosity of the DR specimen (after improvement) has a lower value of 0.19%. In addition, when compared to before and after optimizing the process conditions, all kinds of the porosities showed a large difference, which shows that many improvements were made.

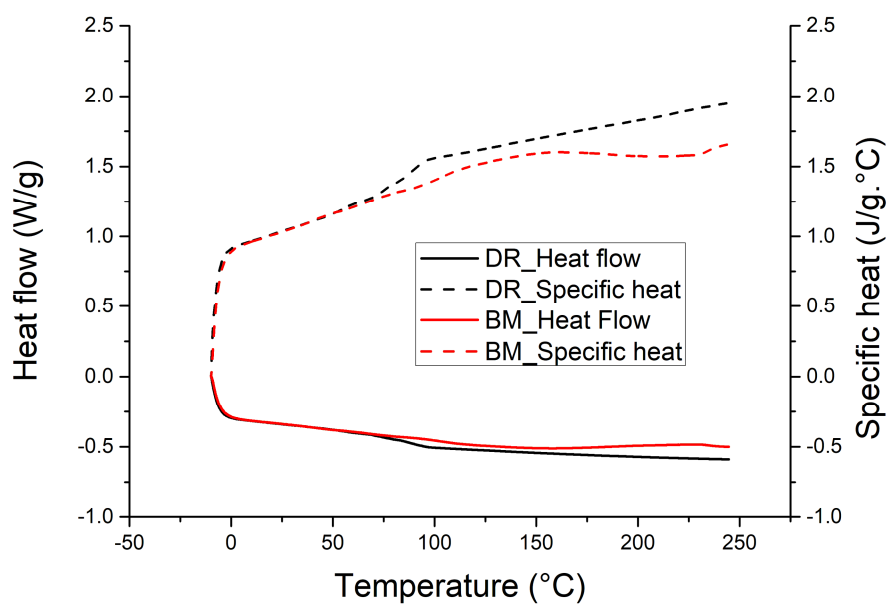


**Figure 2.3.1.** DSC results of the DR product and BM product.



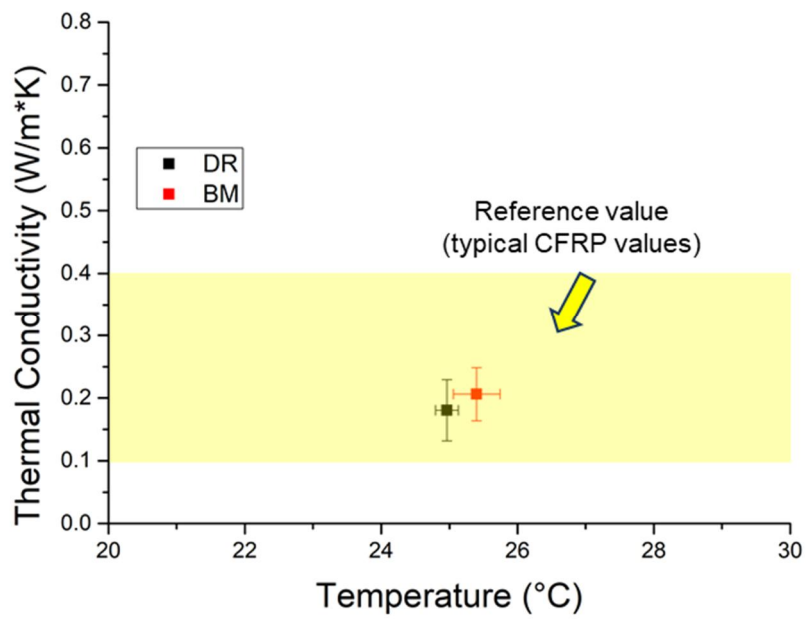


**Figure 2.3.2.** Thermal conductivity of the DR product and BM product.

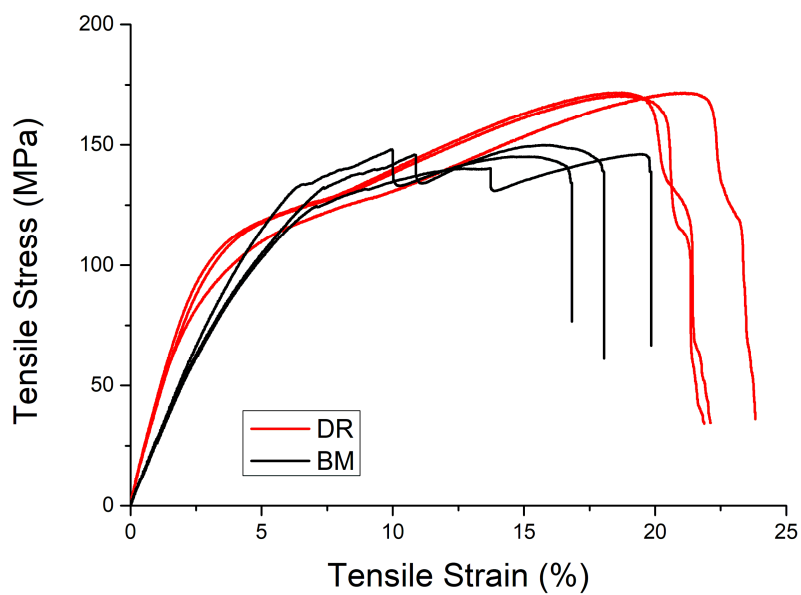


**Figure 2.3.3.** Stress-strain curves of the DR product and BM product for tensile test.

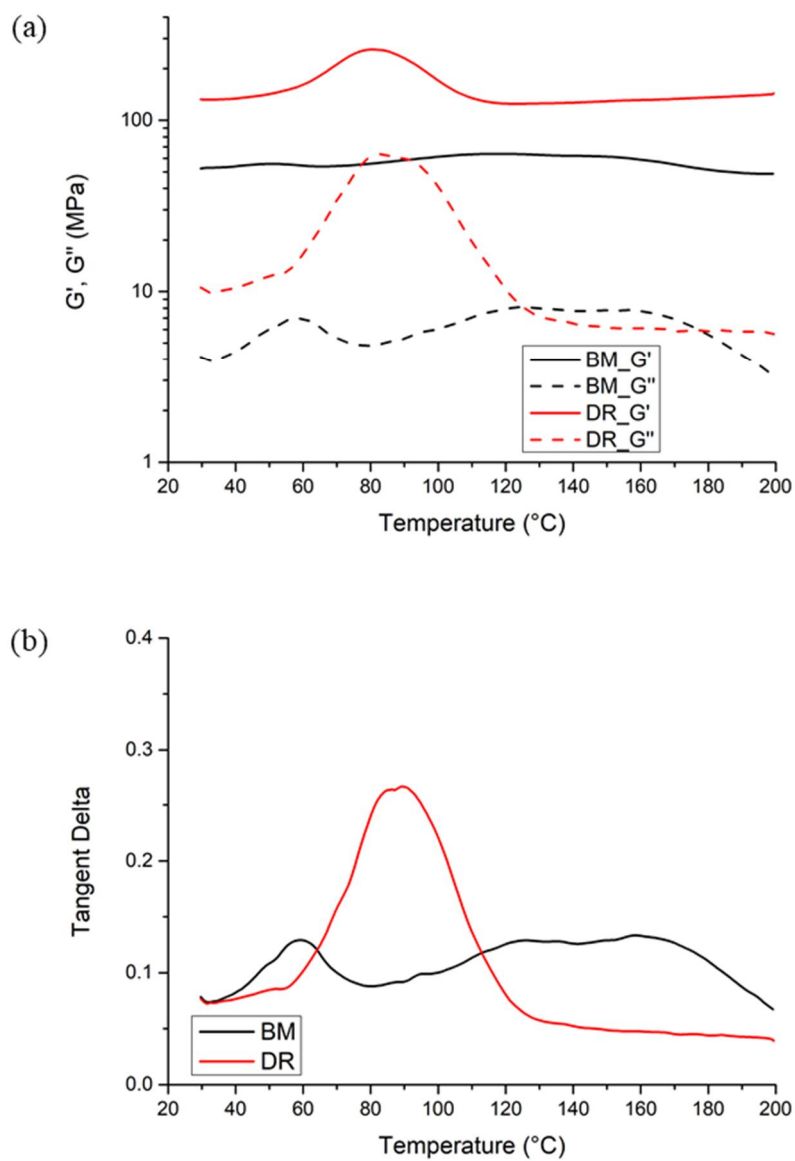


**Figure 2.3.4.** DMA results of the DR product and BM product.

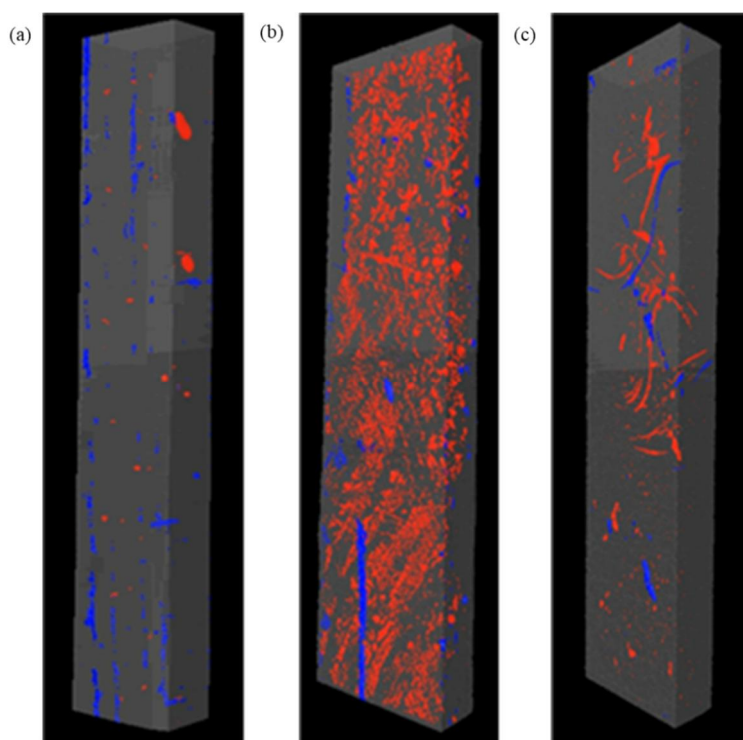


**Figure 2.3.5.** Micro-CT images of the (a) BM product, (b) DR product (before improvement) and (c) DR product (after improvement).

**Table 2.3.1.** Calculated porosity results of BM product, DR product (before improvement) and DR product (after improvement).

	Open porosity (%)	Closed porosity (%)	Total porosity (%)
BM	0.15	0.06	0.21
DR (before improvement)	0.11	0.56	0.67
DR (after improvement)	0.05	0.14	0.19

#### 2.3.4. Summary

A Carbon fiber composite wheel by RTM process was successfully developed and fabricated. Product characterization including thermal, mechanical, viscoelastic and structural analysis were performed. Compared with benchmark rim (BM) product, the reliability of the results was improved. For thermal property, both products had a value of about  $1 \text{ J/g}\cdot^{\circ}\text{C}$  at room temperature. Also, it was difficult to confirm the  $T_g$  because thermosetting polymer was used in both products. At room temperature, the thermal conductivity of DR specimen has a value of  $0.18 \text{ W/m}\cdot\text{K}$ , and the BM specimen has a value of  $0.20 \text{ W/m}\cdot\text{K}$ . Compared with the results of BM specimens, the elastic modulus of the DR specimen was 68%, the tensile strength was 16%, and the elongation rate was 24% higher. To confirm the viscoelastic behavior, the DMA measurement was carried out. DR specimen has a max. storage modulus of 259 MPa at  $81^{\circ}\text{C}$  and a max. loss modulus of 63 MPa at  $83^{\circ}\text{C}$ . And  $T_g$  is about  $80$  to  $95^{\circ}\text{C}$ . On the other hand, the BR specimen has a max. storage modulus of 64 MPa at  $119^{\circ}\text{C}$  and a max. loss modulus of 8 MPa at  $126^{\circ}\text{C}$ .  $T_g$  is about  $62^{\circ}\text{C}$  and  $123^{\circ}\text{C}$ . Micro-CT measurements were performed to confirm the three-dimensional structure. The total porosity of the DR specimen (after improvement) has a lowest value of 0.19%. Compared with benchmark rim (BM), developed rim (DR) mostly have better properties. In addition, the DR product was satisfied various criteria and passed the vehicle test eventually.

### 2.3.5. References

1. Miwa, M.; Endo, I., Critical fibre length and tensile strength for carbon fibre-epoxy composites. *Journal of materials science* **1994**, 29 (5), 1174-1178.
2. Ahlström, J.; Karlsson, B., Modified railway wheel steels: production and evaluation of mechanical properties with emphasis on low-cycle fatigue behavior. *Metallurgical and Materials Transactions A* **2009**, 40 (7), 1557-1567.
3. Nikas, D.; Ahlström, J.; Malakizadi, A., Mechanical properties and fatigue behaviour of railway wheel steels as influenced by mechanical and thermal loadings. *Wear* **2016**, 366, 407-415.
4. Ersoy, N.; Garstka, T.; Potter, K.; Wisnom, M. R.; Porter, D.; Clegg, M.; Stringer, G., Development of the properties of a carbon fibre reinforced thermosetting composite through cure. *Composites Part A: Applied Science and Manufacturing* **2010**, 41 (3), 401-409.
5. Goertzen, W. K.; Kessler, M., Creep behavior of carbon fiber/epoxy matrix composites. *Materials Science and Engineering: A* **2006**, 421 (1-2), 217-225.
6. Cecen, V.; Tavman, I. H.; Kok, M.; Aydogdu, Y., Epoxy and polyester based composites reinforced with glass, carbon and aramid fabrics: Measurement of heat capacity and thermal conductivity of composites by differential scanning calorimetry. *Polymer Composites* **2009**, 30 (9), 1299-1311.
7. Kandare, E.; Khatibi, A. A.; Yoo, S.; Wang, R.; Ma, J.; Olivier, P.; Gleizes, N.; Wang, C. H., Improving the through-thickness thermal and electrical conductivity of carbon fibre/epoxy laminates by exploiting synergy between graphene and silver nano-inclusions. *Composites Part A: Applied Science and Manufacturing* **2015**, 69, 72-82.
8. Rukmini, K.; Ramaraj, B.; Shetty, S. K.; Taraiya, A.; Bandyopadhyay, S., Development of Eco-Friendly Cotton Fabric Reinforced Polypropylene Composites: Mechanical, Thermal, and Morphological Properties. *Advances in Polymer Technology* **2013**, 32 (1).
9. Qi, X.; Yao, X.; Deng, S.; Zhou, T.; Fu, Q., Water-induced shape memory effect of graphene oxide reinforced polyvinyl alcohol nanocomposites. *Journal of Materials Chemistry A* **2014**, 2 (7), 2240-2249.
10. Tan, Y.; Shao, Z.-B.; Yu, L.-X.; Long, J.-W.; Qi, M.; Chen, L.; Wang, Y.-Z., Piperazine-modified ammonium polyphosphate as monocomponent flame-retardant hardener for epoxy resin: flame retardance, curing behavior and mechanical property. *Polymer Chemistry* **2016**, 7 (17), 3003-3012.
11. Margem, F. M.; Monteiro, S. N.; Bravo Neto, J.; Rodriguez, R. J. S.; Soares, B. G., The dynamic-mechanical behavior of epoxy matrix composites reinforced with ramie fibers. *Matéria (Rio de Janeiro)* **2010**, 15 (2), 164-171.
12. Xu, Y.; Zhang, Q.; Zhang, W.; Zhang, P., Optimization of injection molding process parameters to improve the mechanical performance of polymer product against impact. *The International Journal of Advanced Manufacturing Technology* **2015**, 76 (9-12), 2199-2208.

# Chapter 3.

## Injection Molding

### 3.1. Material design

#### 3.1.1. Selection criteria

Thermoplastics are classified as commodity plastics, engineering plastics, and super engineering plastics due to differences in price, market conditions, heat resistance, and mechanical properties<sup>1</sup>. Although the commodity plastics are the most widely used, there is a fatal weakness in thermal properties and mechanical strength. By improving this, engineering plastics are those with a wide range of temperatures and mechanical stresses and properties that can be used for long periods of time in demanding chemical and physical conditions. There are several definitions of engineering plastic, but none has been established yet. One of them is high performance engineering plastic suitable for structural and mechanical parts, mainly for metal replacement, or for industrial applications such as automotive parts, electrical and electronic components, and have a tensile strength more than 50 MPa and a flexural modulus more than 2 GPa and heat resistant to more than 100 °C. And with higher heat resistance, long-term use at temperatures above 150 °C is called super engineering plastic (**Fig. 3.1.1**)<sup>2-4</sup>. However, in order to perform good performance, the degree of difficulty of molding conditions such as molding temperature must be increased accordingly. Therefore, it is more common in the industry to add reinforcements to engineering plastics than to use super engineering plastics<sup>5, 6</sup>.

Carbon fiber (CF), glass fiber, and aramid are widely used as reinforcing materials, and they are approximately 30-40% in weight. CFs have been widely used to reinforce advanced composite materials due to their excellent properties, such as high specific tensile strength, high modulus, and outstanding wear resistance. CFs can be classified as



continuous CFs, long CFs, and short CFs (SCFs) based on the fiber length. CF-reinforced polymers exhibit outstanding mechanical properties and low density and are widely used in the aerospace, transportation, and sporting goods <sup>7</sup>.

In this study, we tried to manufacture wheels with IM process and based on the properties of development product by RTM process. It means that the minimum material properties to be satisfied are 148 MPa for tensile strength, 3 GPa for elastic modulus and 130 °C for maximum temperature. The tensile strength and elastic modulus are the mechanical properties measured by UTM and the temperature is the maximum value actually reached in the rim as measured in the vehicle test. Because it also requires low processability, the resin was chosen as Polyamide6 (PA6) in engineering plastics and the reinforcement was confirmed by carbon fiber. The final combination was determined with 40 wt% carbon fiber filled Polyamide 6 (PA6), as it had the highest tensile strength at 40% pro-content as shown in **Fig.3.1.2** <sup>8</sup>.

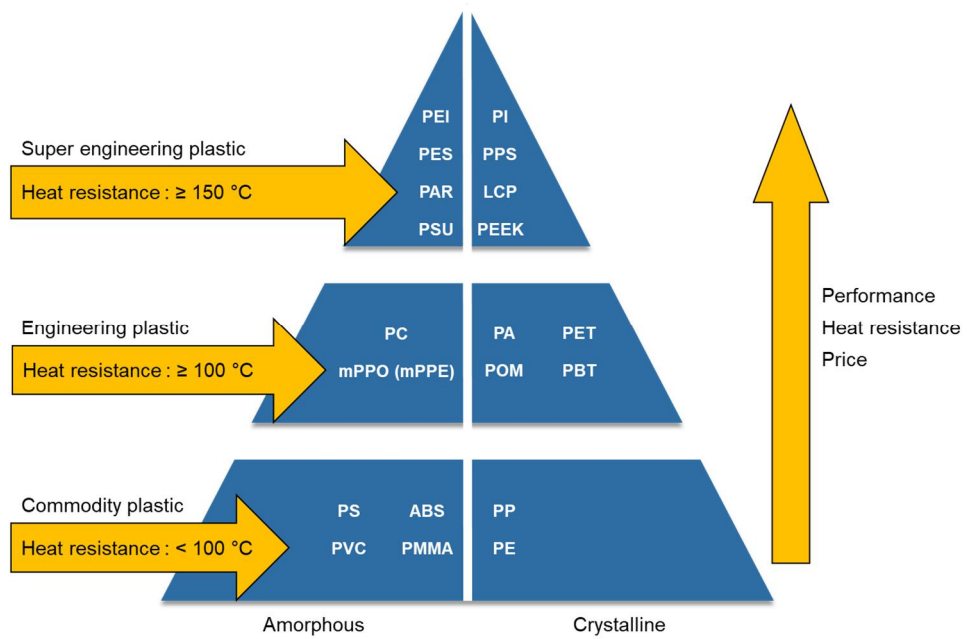


**Figure 3.1.1.** Engineering plastics concept map.

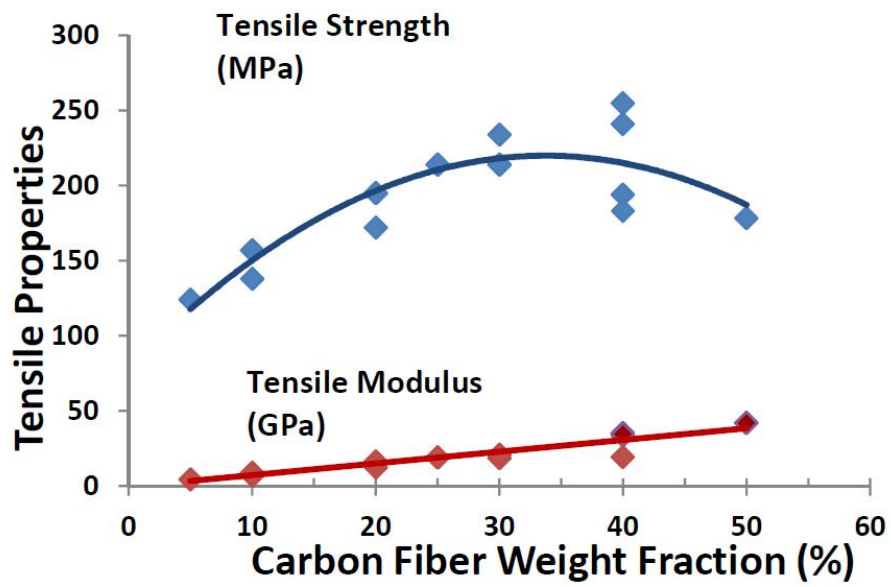


**Figure 3.1.2.** Tensile properties as a function of carbon fiber weight fraction.

### **3.1.2. Summary**

The plastic used in the industry has been summarized and the minimum values of material properties are determined based on the properties of the wheel manufactured by the RTM process. The minimum material properties are 148 MPa for tensile strength, 3 GPa for elastic modulus and 130 °C for maximum temperature. In addition, resin was selected as polyamide6 (PA6) in engineering plastic and reinforced with carbon fiber because it required low processability. The final combination was determined by 40 wt% carbon fiber filled Polyamide 6 (PA6)

### 3.1.3. References

1. Holden, G., Thermoplastic elastomers. In *Rubber technology*, Springer: 1987; pp 465-481.
2. Margolis, J., *Engineering plastics handbook*. McGraw Hill Professional: 2005.
3. Dowling, N. E., *Mechanical behavior of materials: engineering methods for deformation, fracture, and fatigue*. Pearson: 2012.
4. Crawford, R. J., *Plastics engineering*. Elsevier: 1998.
5. Smith, W. F.; Hashemi, J., *Foundations of materials science and engineering*. McGraw-Hill Publishing: 2006.
6. Budinski, K. G.; Budinski, M. K., Engineering materials. *Nature* **2009**, *25*, 28.
7. Yao, S.-S.; Jin, F.-L.; Rhee, K. Y.; Hui, D.; Park, S.-J., Recent advances in carbon-fiber-reinforced thermoplastic composites: A review. *Composites Part B: Engineering* **2018**, *142*, 241-250.
8. Geldernick, J.; Bergler, N.; Mathur, R., EXPANDING DESIGN OPTIONS FOR LONG FIBER THERMOPLASTIC COMPOSITES.

## **3.2. Numerical simulation**

### **3.2.1. Introduction**

Reducing fuel efficiency becomes an important issue in the automotive industry. For this, hybrid engines and lightweight components are applied to automobiles. Among them, reducing weight of the wheel by employing the composite rim is one of challenging issues. In recent years, the wheels have been manufactured using fiber reinforced composites, but it is still not feasible to produce them by injection molding <sup>1,2</sup>

Injection molding is a cost and time efficient processing method for mass production of polymeric parts. It is also environmentally friendly compared with other methods since it uses thermoplastic polymer in a closed environment. It has recently been used to produce parts with complex shapes and small dimensions such as micro- and nano- scales <sup>3-5</sup>. Injection molding process can be modeled numerically to understand the entire steps such as filling, packing, cooling, and ejection stages <sup>6-20</sup>. Numerical simulation will save cost and time in designing and manufacturing polymeric parts by optimizing processing conditions.

In this study, numerical analysis was carried out to manufacture a thick and complex automotive wheel with carbon fiber composite. The resin flow during filling and deformation of parts at ejection were predicted numerically. Insert injection molding was also considered to reduce the deformation of the part and improve the mechanical properties. The insert injection molded part was assessed in terms of pressure, fiber orientation, deformation, elastic modulus, and residual stress distribution.

### 3.2.2. Numerical analysis

A finite element method (FEM) simulation program, Moldex3D<sup>®</sup>, was used in this study. The entire processing steps, filling, packing, cooling, and warpage stages, were modeled for injection molding of carbon fiber composite automotive wheels. The resin flow in the mold is governed by the following equations <sup>21</sup>.

$$\frac{d\rho}{dt} + \rho(\nabla \cdot \mathbf{u}) = 0 \quad (3.2.1)$$

$$\rho \frac{d\mathbf{u}}{dt} = -\nabla P + \nabla \cdot \tilde{\boldsymbol{\tau}} + \rho \mathbf{g} \quad (3.2.2)$$

$$\rho C_p \frac{dT}{dt} = \beta T \frac{dP}{dt} + \eta \tilde{\gamma}^2 + \nabla \cdot \mathbf{q} \quad (3.2.3)$$

, where  $\rho$  is the density,  $\mathbf{u}$  is the velocity vector,  $P$  is the pressure,  $\tilde{\boldsymbol{\tau}}$  is the stress tensor,  $\mathbf{g}$  is the gravity vector,  $C_p$  is the specific heat at constant pressure,  $\beta$  is the thermal expansion coefficient,  $\eta$  is the generalized Newtonian viscosity,  $\mathbf{q}$  is the heat flux vector, and  $\tilde{\gamma}$  is the magnitude of shear rate tensor.

The magnitude of shear rate tensor,  $\tilde{\gamma}$  in the Cartesian coordinate system as below:

$$\tilde{\gamma} = \sqrt{\left(\frac{\partial u}{\partial z}\right)^2 + \left(\frac{\partial v}{\partial z}\right)^2} \quad (3.2.4)$$

, where (u, v) are the velocity components in the (x, y) directions.

In this case, the modified-Cross model is used to describe the viscosity of polymer melt:

$$\eta(T, \dot{\gamma}, P) = \frac{\eta_0(T, P)}{1 + \left(\frac{\eta_0(T, P) \tilde{\gamma}}{\tau^*}\right)^{1-n}} \quad (3.2.5)$$

, where  $\eta$  is the viscosity,  $\eta_0$  is the zero shear rate viscosity,  $\tau^*$  is the shear stress at the transition between the Newtonian and the Power-law behaviors, and  $n$  is the Power-law index.

The zero shear rate viscosity,  $\eta_0$  can be represented as a function of temperature using the Williams-Landel-Ferry (WLF) equation:

$$\eta_0(T, P) = D_1 \exp\left(-\frac{A_1(T - T^*(P))}{A_2 + D_3P + (T - T^*(P))}\right) \quad (3.2.6)$$

, where  $T^*(P) = D_2 + D_3P$ . The material constants for **Eqns. (3.2.5) and (3.2.6)** are taken from Moldex3D.

A volume fraction function  $f$  is introduced to track the evolution of the melt front. Here,  $f=0$  is defined as the air phase,  $f=1$  as the polymer melt phase, and then the melt front is located within cells with  $0 < f < 1$ . The advancement of  $f$  over time is governed by the following transport equation:

$$\frac{\partial f}{\partial t} + \nabla \cdot (\mathbf{u}f) = 0 \quad (3.2.7)$$

**Fig. 3.2.1(a)** shows the shape of the automotive wheel. Geometric modeling and finite element generation were carried out (**Fig. 3.2.1(b)~(d)**). More than 2 million finite elements were generated by employing tetrahedral, prism, pyramid, and hexagonal elements. The diaphragm gate was selected (**Fig. 3.2.2(a)**) and the size and shape of the sprue, gate, and runner were determined. As shown in **Fig. 3.2.2(b)**, the conformal cooling channel was considered and the nine cooling lines have the spiral structure. The entire mold has a size of 1200 mm × 1200 mm × 1200 mm (**Fig. 3.2.2(c)**). For numerical simulation, two cases were taken into account: Case 1 without insert and Case 2 with metallic insert (**Fig. 3.2.3**). The insert parts were positioned at upper and lower locations in the automotive wheel as shown in **Fig. 3.2.3(b)**. 40 wt% carbon fiber filled Polyamide 6 (PA6) (Akro-plastic Corporation (AKROMID B3 ICF 40)) and aluminum insert were taken into account for the simulation. The material properties for numerical analysis were obtained from Moldex3D. Processing conditions are listed in **Table 3.2.1**.



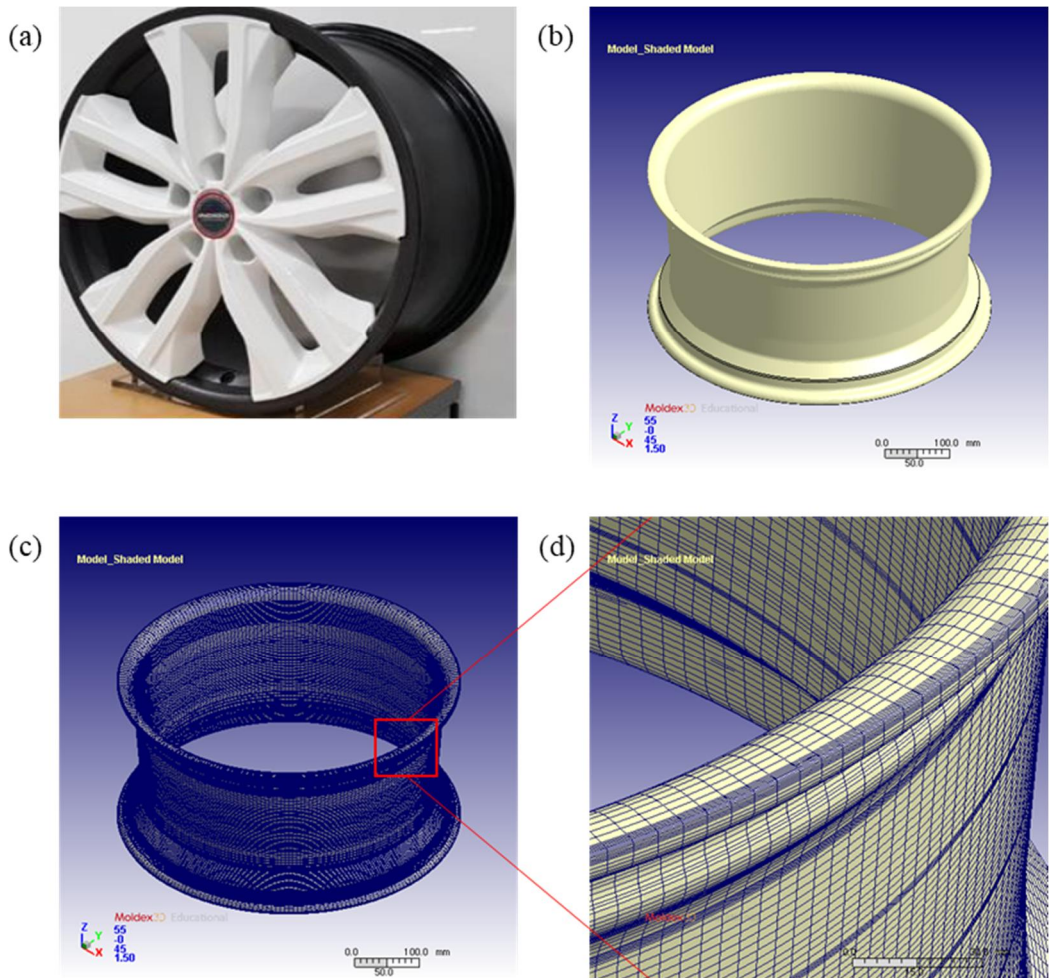


**Figure 3.2.1.** (a) Automotive wheel considered in this study, (b) CAD model, (c) finite element mesh, and (d) magnified mesh structure.

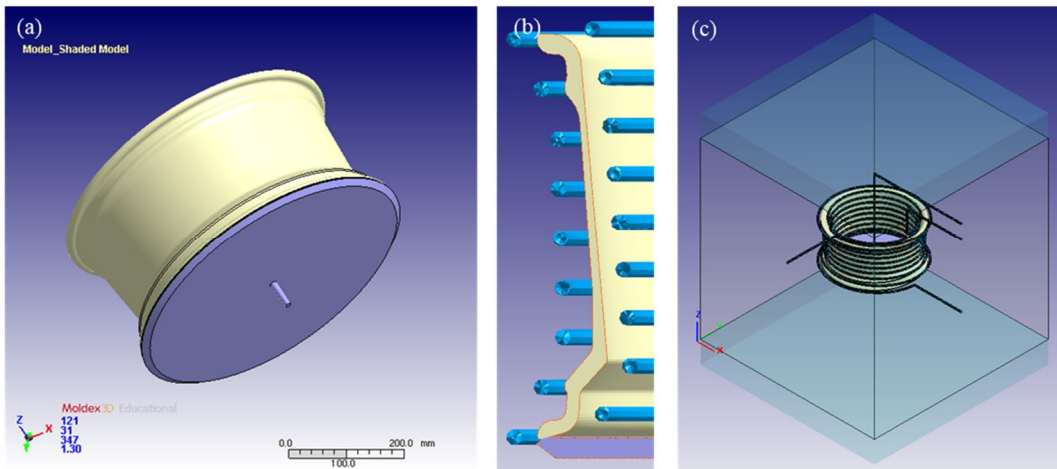


**Figure 3.2.2.** Geometry of (a) runner and gate, (b) cooling channel, and (c) mold.

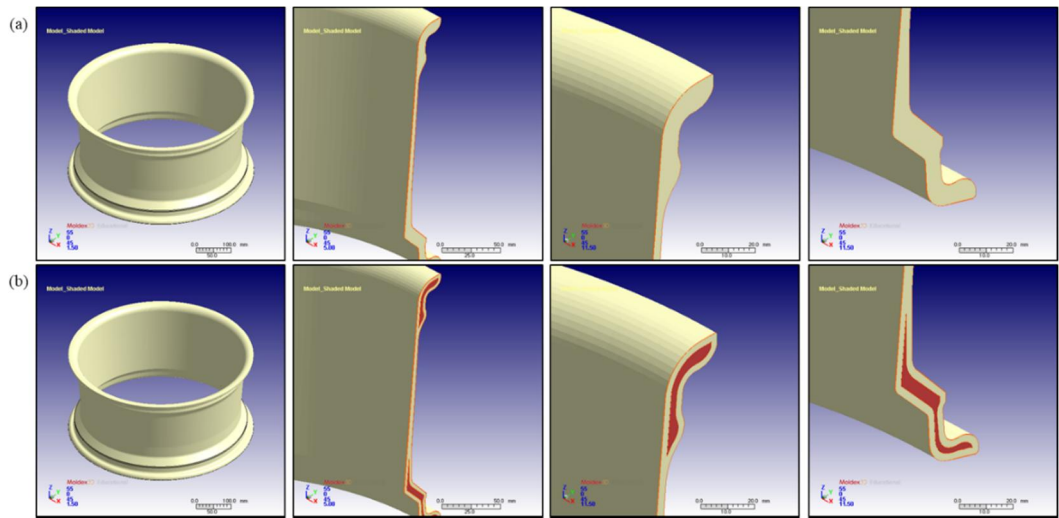


**Figure 3.2.3.** Geometry of (a) Case 1 without insert and (b) Case 2 with insert.

**Table 3.2.1.** Process conditions used in the simulation.

	w/o insert	w/ insert
Filling time	7 s	1.5 s
Packing time	70 s	55 s
Cooling time	900 s	
Melt temperature	285 °C	
Initial insert part temperature	-	80 °C
Mold temperature	80 °C	
Freeze temperature	186 °C	
Ejection temperature	166 °C	

### 3.2.3. Results and discussion

The sprue pressure required to fill the cavity is shown as a function of the filling time in **Fig. 3.2.4**. High melt velocity needs high injection pressure to fill the mold cavity and high sprue pressure is required to achieve short filling time. The sprue pressure showed a minimum value in the graph for the cases without and with insert with respect to the filling time, which allowed us to determine the optimum filling times (i.e., 7 s without insert and 1.5 s with insert). The freezing time at the gate was also predicted by the simulation. The packing time without and with insert was 70 s and 55 s, respectively (**Fig. 3.2.5**). The initial temperature of the aluminum insert was set at 80 °C. Since minimum cooling time typically indicates the time when 80% of cavity and 60% of runner are cooled, the cooling time was increased to 900s.

**Fig. 3.2.6** shows the melt front advancement in the cavity with respect to time. The resin filled the circular runner first and infused the cavity. The filling time was 7.077 s for Case 1 and 1.514 s for Case 2. Higher pressure was required for Case 2 because its filling time was shorter than that of Case 1. Therefore, Case 2 showed higher pressure field than Case 1 as shown in **Fig. 3.2.7 (a~b)**. Total weight of Case 2 was higher than that of Case 1 (**Fig. 3.2.7(c)**) because the density of aluminum (i.e.,  $2.7 \times 10^3 \text{ kg/m}^3$ ) is higher than that of polymer (i.e.,  $1.31 \times 10^3 \text{ kg/m}^3$ ).

The fiber orientation was predicted as shown in **Fig. 3.2.8**. Since the resin mainly flowed in the vertical direction, fibers were oriented along that direction in both cases (**Fig. 3.2.8**). It was found that the two cases had quite similar fiber orientation.

**Fig. 3.2.9** presents the elastic modulus of the molded part in x, y and z directions. The average modulus in each direction is given in the figure. Case 2 with insert showed higher values in every direction because of the aluminum insert. The elastic modulus of aluminum is 68 GPa, and that of the carbon fiber is 38.2 GPa in the longitudinal direction and 10.3 GPa in the transverse direction. For both cases, the modulus in the z direction is higher than that in the x and y directions due to the fiber orientation.

The total deformation and thermal residual stress of the molded part are shown in **Fig. 3.2.10**. For Case 1, the deformation increased as the distance from the gate became larger (**Fig. 3.2.10(a)**). It was found in Case 2 that the deformation was significantly

reduced at the upper and lower locations where the insert part was located (**Fig. 3.2.10(b)**). However, the deformation in the middle was increased to 2.5 mm. On the other hand, the residual stress of Case 2 was higher than that of Case 1, especially in the middle region. Consequently, the molded rim with insert achieved significant improvement in the deformation.

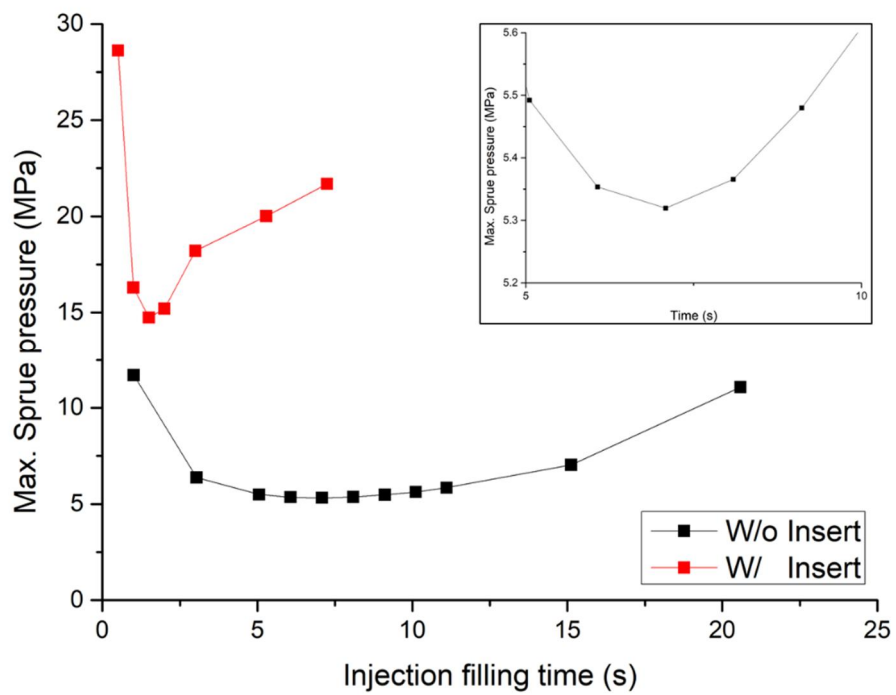


**Figure 3.2.4.** Sprue pressure w.r.t. the filling time.

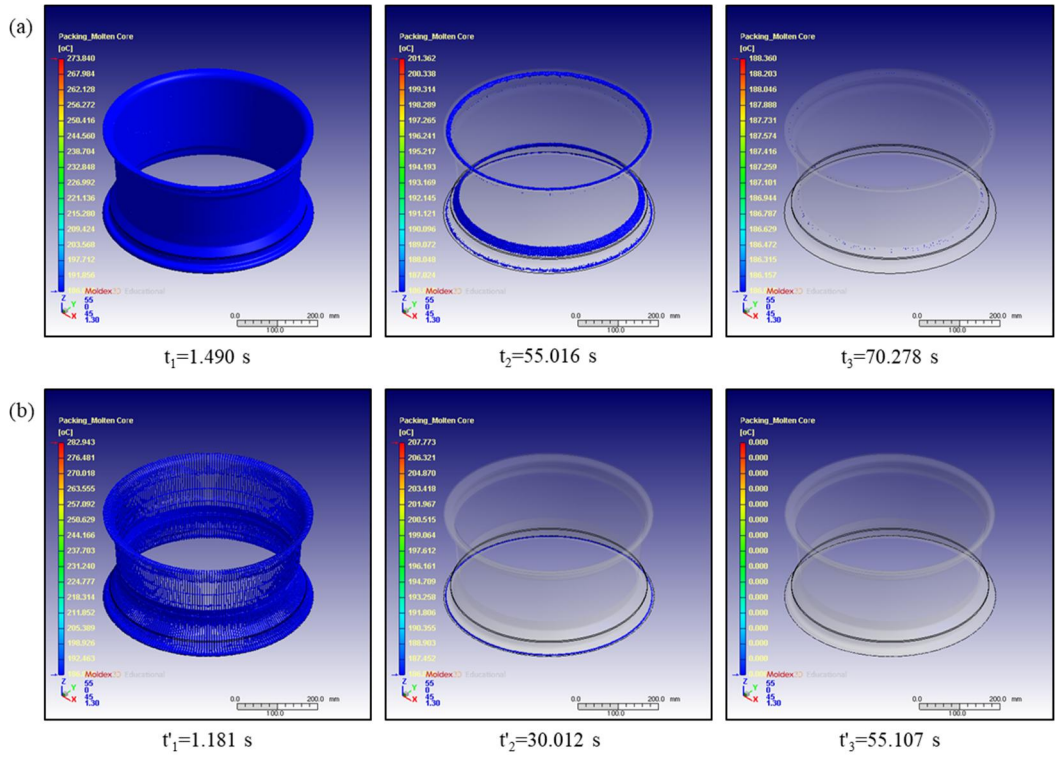


**Figure 3.2.5.** Existing polymer melt w.r.t. time: (a) Case 1 and (b) Case 2.



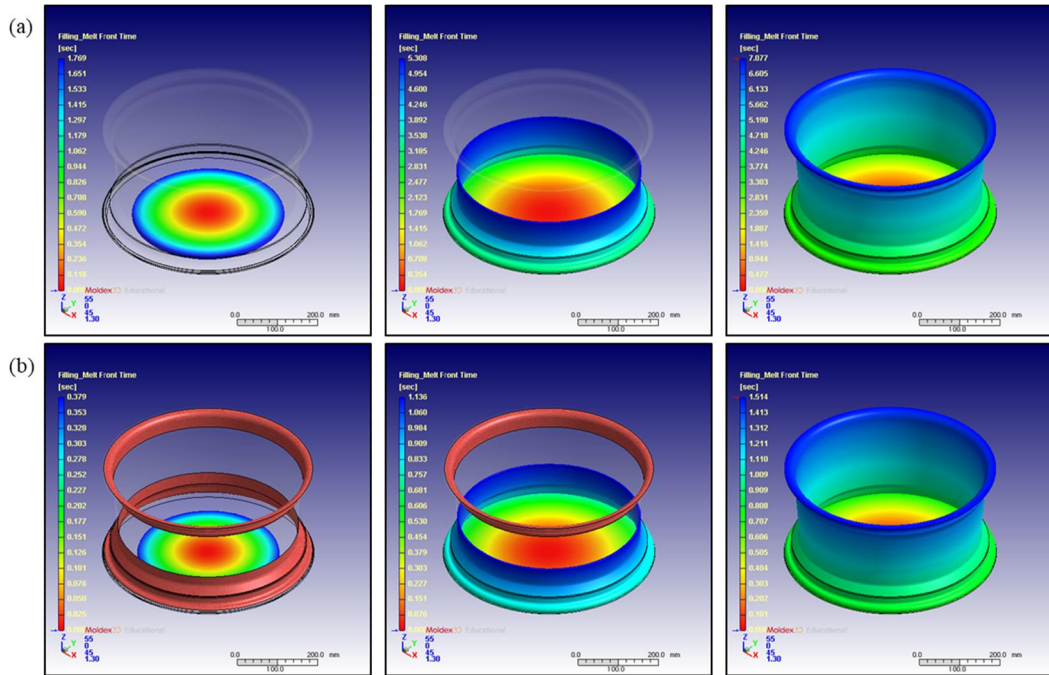


**Figure 3.2.6.** Melt front advancement in the cavity w.r.t. time: (a) Case 1 and (b) Case 2 at 25%, 75%, and 100% filling.

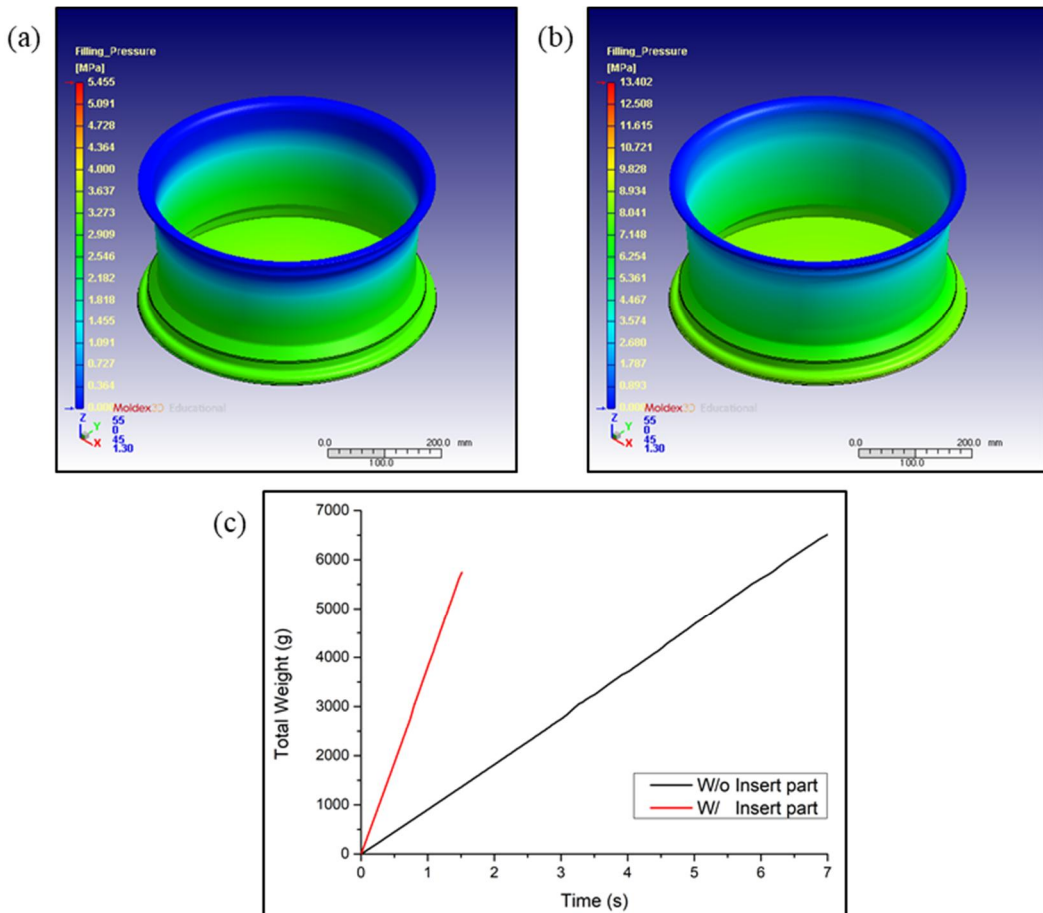


**Figure 3.2.7.** Pressure distribution after 100% filling: (a) Case 1, (b) Case 2, (c) Comparison of the total weight between the two cases.



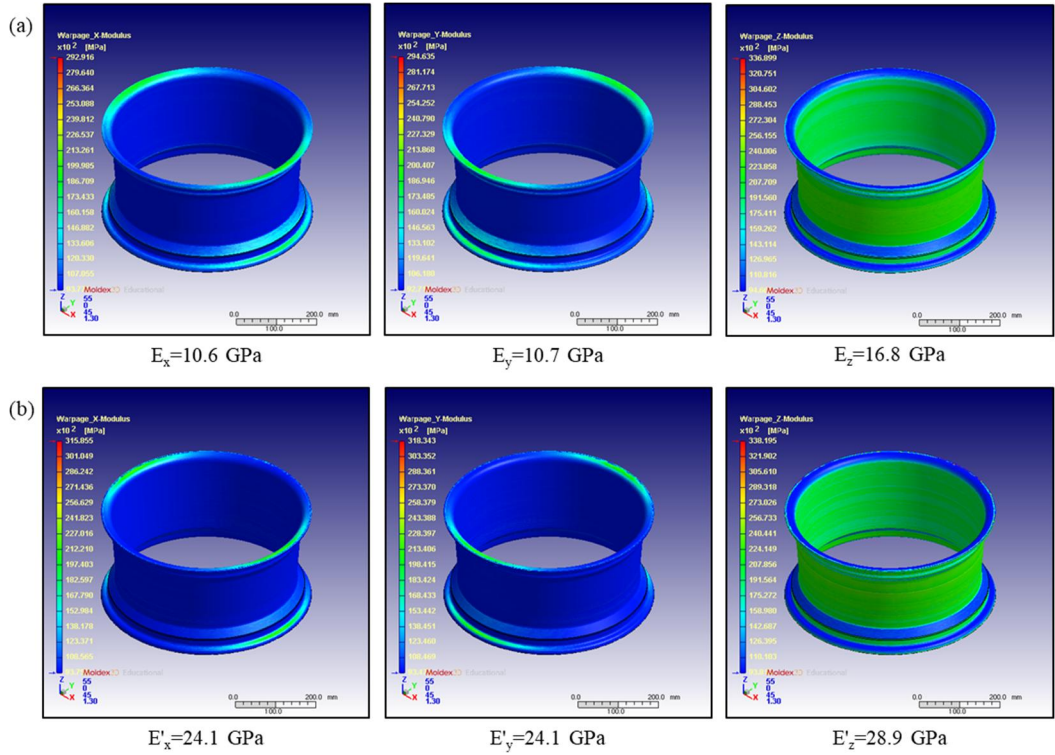


**Figure 3.2.9.** Elastic modulus of the molded part in the x, y and z direction: (a) Case 1 and (b) Case 2.

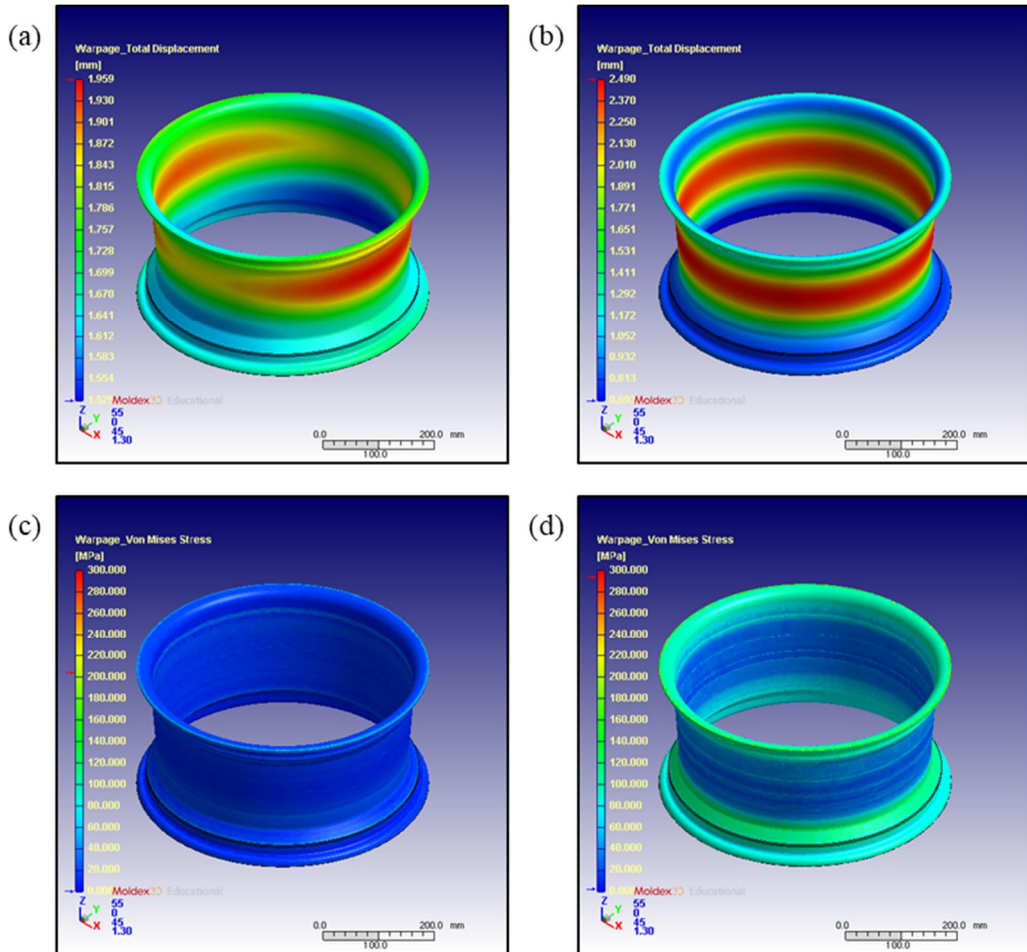


**Figure 3.2.10.** Total deformation and thermal residual stress of the molded part for Case 1 ((a) and (c)) and Case 2 ((b) and (d)).

#### **3.2.4. Summary**

3D numerical simulation of injection molding was carried out for automotive wheel. The resin flow and warpage of the product were investigated numerically. The filling time in the cavity was optimized and the gate freezing time was determined. The effect of insert on the injection-molded part was also evaluated. It was found that the deformation of the part was significantly reduced when the insert was applied. This study will provide a meaningful guideline for manufacturing a real automotive wheel via injection molding.

### 3.2.5. References

1. Hong, J.-H.; Yoo, S.-H.; Chang, S.-H., Design and performance evaluation of carbon fiber/epoxy composite-aluminum hybrid wheel for passenger cars. *Composites Research* **2013**, 26 (6), 386-391.
2. Xiaoyin, W.; Xiandong, L.; Yingchun, S.; Xiaofei, W.; Wanghao, L.; Yue, P., Lightweight design of automotive wheel made of long glass fiber reinforced thermoplastic. *Proceedings of the Institution of Mechanical Engineers, Part C: Journal of Mechanical Engineering Science* **2016**, 230 (10), 1634-1643.
3. Bellantone, V.; Surace, R.; Trotta, G.; Fassi, I., Replication capability of micro injection moulding process for polymeric parts manufacturing. *The international journal of advanced manufacturing technology* **2013**, 67 (5-8), 1407-1421.
4. Lucchetta, G.; Sorgato, M.; Carmignato, S.; Savio, E., Investigating the technological limits of micro-injection molding in replicating high aspect ratio micro-structured surfaces. *CIRP Annals* **2014**, 63 (1), 521-524.
5. Oh, H. J.; Song, Y. S., Precise nanoinjection molding through local film heating system. *RSC Advances* **2015**, 5 (121), 99797-99805.
6. Kitayama, S.; Yokoyama, M.; Takano, M.; Aiba, S., Multi-objective optimization of variable packing pressure profile and process parameters in plastic injection molding for minimizing warpage and cycle time. *The International Journal of Advanced Manufacturing Technology* **2017**, 92 (9-12), 3991-3999.
7. Jahan, S. A.; Wu, T.; Zhang, Y.; Zhang, J.; Tovar, A.; Elmounayri, H., Thermo-mechanical design optimization of conformal cooling channels using design of experiments approach. *Procedia Manufacturing* **2017**, 10, 898-911.
8. Laurenzi, S.; Grilli, A.; Pinna, M.; De Nicola, F.; Cattaneo, G.; Marchetti, M., Process simulation for a large composite aeronautic beam by resin transfer molding. *Composites Part B: Engineering* **2014**, 57, 47-55.
9. Li, X.; Gong, N.; Gao, Z.; Yang, C., Fiber orientation in melt confluent process for reinforced injection molded part. *The International Journal of Advanced Manufacturing Technology* **2017**, 90 (5-8), 1457-1463.
10. Kim, B.; Min, J., Residual stress distributions and their influence on post-manufacturing deformation of injection-molded plastic parts. *Journal of Materials Processing Technology* **2017**, 245, 215-226.
11. Zhou, H., Computer modeling for injection molding. *Simulation, Optimization, and Control* **2013**.
12. Wang, Y.; Yu, K.-M.; Wang, C. C., Spiral and conformal cooling in plastic injection molding. *Computer-Aided Design* **2015**, 63, 1-11.
13. Azaman, M.; Sapuan, S.; Sulaiman, S.; Zainudin, E.; Khalina, A., Shrinkages and warpage in the processability of wood-filled polypropylene composite thin-walled parts formed by injection molding. *Materials & Design (1980-2015)* **2013**, 52, 1018-1026.
14. Hsu, F.; Wang, K.; Huang, C.; Chang, R., Investigation on conformal cooling system design in injection molding. *Advances in Production Engineering & Management* **2013**, 8 (2), 107-115.
15. Mohamed, O. A.; Masood, S.; Saifullah, A., A simulation study of conformal cooling channels in plastic injection molding. *International Journal of Engineering*

*Research* **2013**, 2 (5), 344-348.

16. Xu, Y.; Zhang, Q.; Zhang, W.; Zhang, P., Optimization of injection molding process parameters to improve the mechanical performance of polymer product against impact. *The International Journal of Advanced Manufacturing Technology* **2015**, 76 (9-12), 2199-2208.
17. Spina, R.; Spekowius, M.; Dahlmann, R.; Hopmann, C., Analysis of polymer crystallization and residual stresses in injection molded parts. *International journal of precision engineering and manufacturing* **2014**, 15 (1), 89-96.
18. Oliaei, E.; Heidari, B. S.; Davachi, S. M.; Bahrami, M.; Davoodi, S.; Hejazi, I.; Seyfi, J., Warpage and shrinkage optimization of injection-molded plastic spoon parts for biodegradable polymers using taguchi, ANOVA and artificial neural network methods. *Journal of Materials Science & Technology* **2016**, 32 (8), 710-720.
19. Azaman, M.; Sapuan, S.; Sulaiman, S.; Zainudin, E.; Khalina, A., Optimization and numerical simulation analysis for molded thin-walled parts fabricated using wood-filled polypropylene composites via plastic injection molding. *Polymer Engineering & Science* **2015**, 55 (5), 1082-1095.
20. Khan, M.; Afaq, S. K.; Khan, N. U.; Ahmad, S., Cycle time reduction in injection molding process by selection of robust cooling channel design. *ISRN Mechanical Engineering* **2014**, 2014.
21. Kwon, Y. I.; Song, Y. S., Application of injection-compression molding to thin-walled polymeric parts. *Korea-Australia Rheology Journal* **2018**, 30 (3), 161-167.



### **3.3. Specimen production and characterization**

#### **3.3.1. Introduction**

To manufacture the specimen by injection molding process, an injection machine for lab-scale called HAAKE™ MiniJet Pro Piston Injection Molding System was employed <sup>1</sup>. The test specimen can be fabricated with only a small amount of various materials, including powder, pellets or melts. Interchangeable molds allow specimens to be produced from standard to customized shapes. The ease of use is also excellent, such as the mold can be replaced without tools.

The thermal, mechanical, and viscoelastic properties of the specimens were measured as in the RTM process study. However, PA6 as the thermoplastic resin used in this study showed different material properties than epoxy, which is a thermosetting resin used in previous study <sup>2-6</sup>.

Thermoplastics are easily softened and become sticky liquid when they are heated. It is natural that when the heat is continuously applied, each molecule is dispersed and vaporized separately. However, because of its high molecular weight, it requires a considerably high temperature for vaporization. If heated more strongly, it will cause thermal decomposition of the polymer. Then, it is processed by heating it only to the temperature of the sticky liquid state <sup>7-10</sup>.

### 3.3.2. Experimental section

The entire progress for fabrication of dog-bone specimen by injection molding is shown in **Fig. 3.3.1**. 40 wt% carbon fiber filled Polyamide 6 (PA6) (Hyosung Corporation (Brt 1011)) as the combination determined in previous study was fabricated. In addition, pure PA6 was also manufactured for comparison. Detailed process conditions are listed in the **Table. 3.3.1**.

The thermal, mechanical, viscoelastic and structural characteristics of the developed specimens were evaluated. Glass transition temperature and thermal stability were measured to evaluate the thermal properties of the developed products. The specimens were made to fit the pan for the measurement equipment. Glass transition temperature was measured by Differential Scanning Calorimeter (DSC). The test conditions were as follows: the temperature range was from -20 to 250 °C, and the heating rate was 10 °C/min.

Thermal Gravimetric Analysis (TGA) was conducted to measure the thermal stability. . The specimens were also made as powder to fit the measurement equipment requirement. The temperature range for the test conditions was from 25 to 600 °C.

The elastic modulus and tensile strength measurements were carried out using Universal Testing Machine (UTM). The specimen size is 250 mm (L) × 3 mm (W) × 3 mm (T) in dog-bone form. The tensile speed for the test conditions is 10 mm / min.

The storage and loss modulus measurements were performed using Dynamic Mechanical Analysis (DMA). The method of measurement was a compression method and the specimen was made with the dimension of 10 mm × 10 mm. The test conditions were as follows: oscillatory force is 10 N, displacement is 10 μm, frequency is 1 Hz, temperature range was from 30 to 300 °C and heating rate was 3 °C/min.

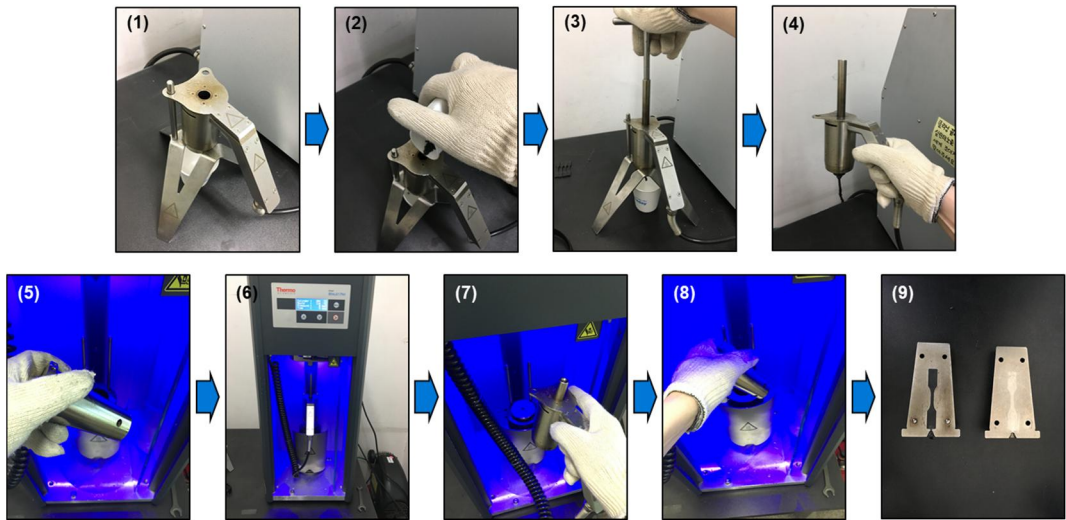


**Figure 3.3.1.** Experimental progress for fabrication of PA/40CF specimen.

**Table 3.3.1.** Process conditions for the experiments.

	PA/40CF	PA
Cylinder temperature	280 °C	250 °C
Mold temperature	110 °C	
Injection pressure	400 bar	
Injection time	5 s	
Packing pressure	200 bar	
Packing time	5 s	

### 3.3.3. Results and discussion

**Fig. 3.3.2** shows 40wt% carbon fiber filled PA6 (PA/40CF) and pure PA6 (PA) specimens by injection molding. As shown in **Fig. 3.3.2**, two molds with dog-bone and bar shapes were used.

The  $T_g$  was obtained from the heat flow value according to the temperature as shown in **Fig. 3.3.3**. As a result, the  $T_g$  is about 222 °C in both specimens. **Fig. 3.3.4** shows the TGA results that the weights of both samples started to decrease from about 380 °C. Final weight percent is 40.9% for PA/40CF and 0.77% for pure PA.

**Fig. 3.3.5** shows the stress-strain curve (s-s curve) after three tensile tests, showing a relatively low deviation between specimens. The elastic modulus is calculated in the elongation range of 0.05 to 0.25%, and the elastic moduli of PA/40CF and PA specimens are 13.77 GPa and 5.90 GPa, respectively. The s-s curve shows a tensile strength of 209.27 MPa when the elongation of the PA/40CF specimen is 5.20%. The pure PA specimen has a tensile strength of 57.13 MPa when the elongation is about 12%.

The DMA results (**Fig. 3.3.6**) show that the storage moduli and loss moduli of the both cases are stable until about 200 °C. PA6/40CF specimen has a max. storage modulus of 71.22 MPa at 212.8 °C and a max. loss modulus of 48.67 MPa at 215.6 °C. And  $T_g$  is about 215.6 °C. On the other hand, the pure PA specimen has a max. storage modulus of 35.52 MPa at 205.2 °C and a max. loss modulus of 22.45 MPa at 212.1 °C.  $T_g$  is about 212.1 °C.

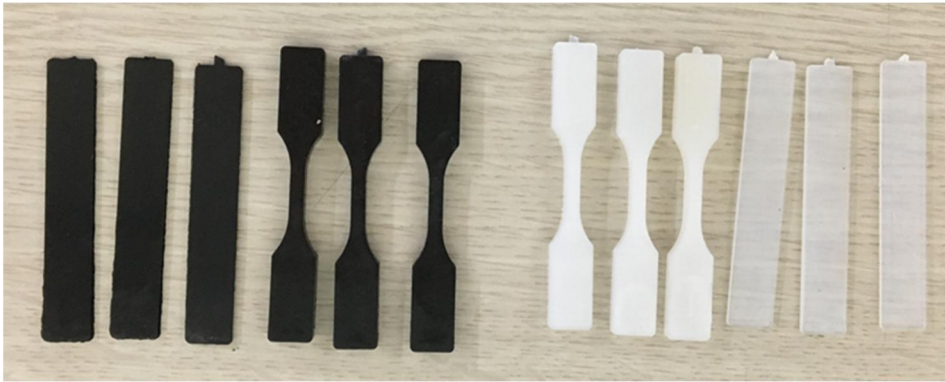


**Figure 3.3.2.** PA/40CF and PA specimens by injection molding

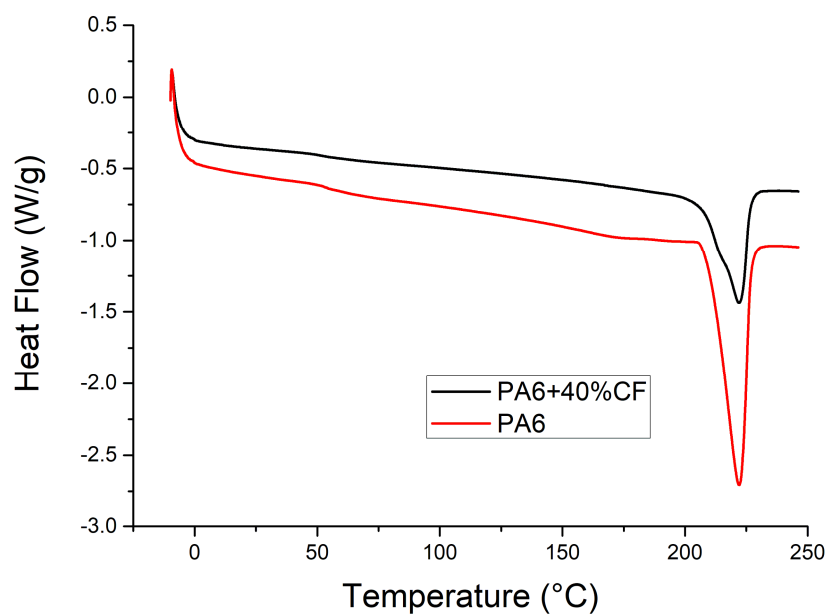


**Figure 3.3.3.** DSC results of PA/40CF and pure PA specimens.

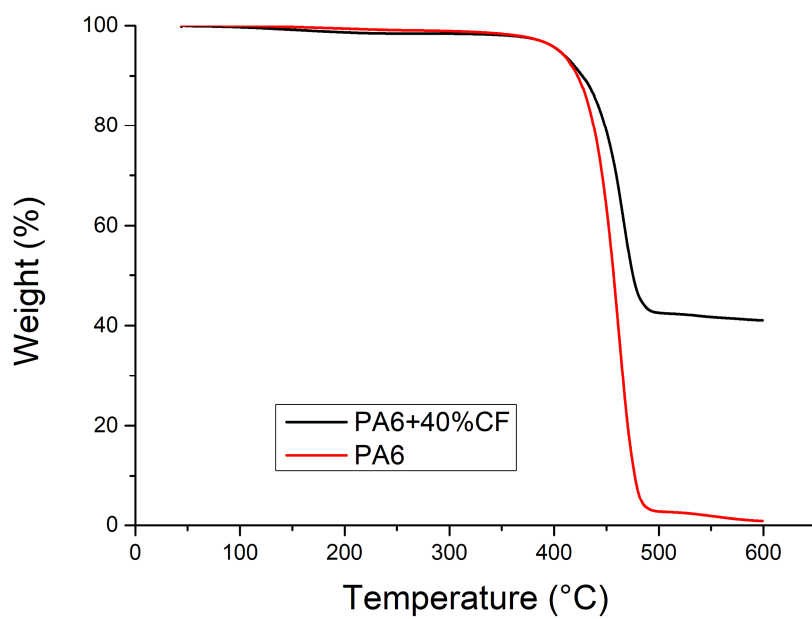


**Figure 3.3.4.** TGA results of PA/40CF and pure PA specimens.



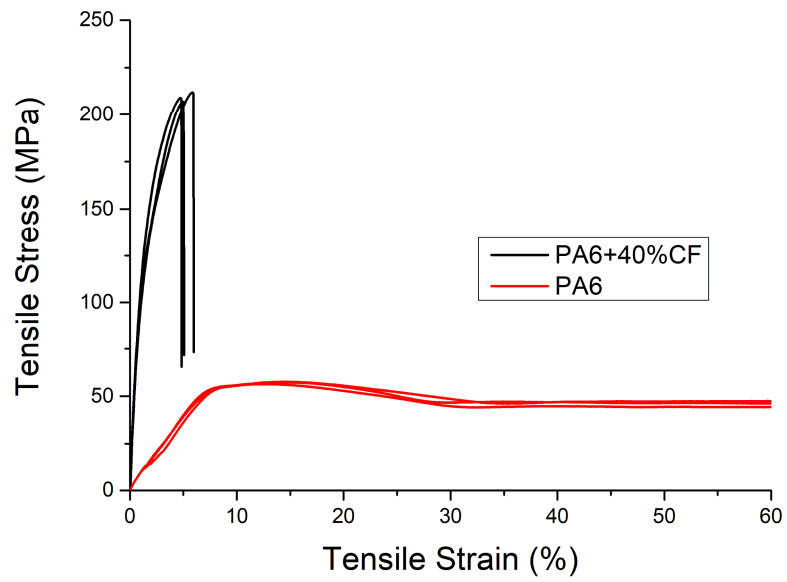


**Figure 3.3.5.** Stress-strain curves of the PA/40CF and pure PA specimens for tensile test.

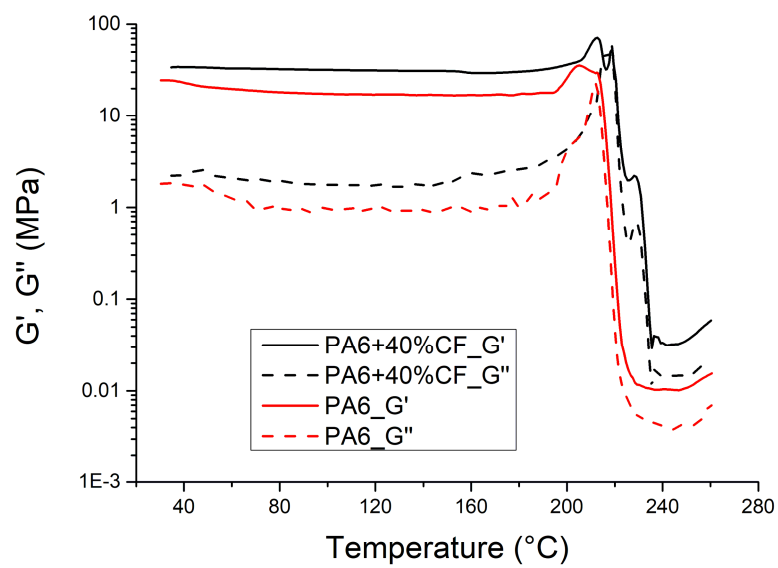


**Figure 3.3.6.** DMA results of the PA/40CF and pure PA specimens.

### **3.3.4. Summary**

A Carbon fiber composite specimen by IM process was successfully developed and fabricated. Product characterization including thermal, mechanical and viscoelastic were performed. Compared with pure PA6 specimen and product manufactured with RTM process, the reliability of the results was improved. For thermal property, both specimens had a T<sub>g</sub> value of about 222 °C. The elastic modulus of the PA/40CF specimen was 13.77 GPa, the tensile strength was 209.27 MPa, which is much higher than pure Pa6 and product manufactured with RTM process. To confirm the viscoelastic behavior, the DMA measurement was carried out. PA/40CF specimen has a max. storage modulus of 71.22 MPa at 212.8 °C and a max. loss modulus of 48.67 MPa at 215.6 °C. And T<sub>g</sub> is about 215.6. It also found that the most measured material properties of PA/CF specimen were higher than those of benchmark and developed products made with RTM. It means that these results can suggest the possibility of actual injection molding processing

### 3.3.5. References

1. Fisher, S. T., HAAKE™ MiniJet Pro Piston Injection Molding System. *Thermo Scientific, Waltham, MA*, accessed Jan **2015**, 5, 2016.
2. Mahallati, P.; Arefazar, A.; Naderi, G., Thermal and morphological properties of thermoplastic elastomer nanocomposites based on PA6/NBR. **2011**.
3. Han, K. q.; Liu, Z. j.; Yu, M. h., Preparation and mechanical properties of long glass fiber reinforced PA6 composites prepared by a novel process. *Macromolecular Materials and Engineering* **2005**, 290 (7), 688-694.
4. Malchev, P. G.; David, C. T.; Picken, S. J.; Gotsis, A. D., Mechanical properties of short fiber reinforced thermoplastic blends. *Polymer* **2005**, 46 (11), 3895-3905.
5. Li, J.; Xia, Y., The friction and wear properties of thermoplastic PA6 composites filled with carbon fiber. *Journal of Thermoplastic Composite Materials* **2010**, 23 (3), 337-349.
6. Cartledge, H. C.; Baillie, C.; Mai, Y.-W., Friction and wear mechanisms of a thermoplastic composite GF/PA6 subjected to different thermal histories. *Wear* **1996**, 194 (1-2), 178-184.
7. Clegg, D.; Collyer, A., *Mechanical properties of reinforced thermoplastics*. Springer: 1986; Vol. 326.
8. Park, H.-M.; Lee, W.-K.; Park, C.-Y.; Cho, W.-J.; Ha, C.-S., Environmentally friendly polymer hybrids Part I Mechanical, thermal, and barrier properties of thermoplastic starch/clay nanocomposites. *Journal of Materials Science* **2003**, 38 (5), 909-915.
9. Barick, A.; Tripathy, D., Effect of organically modified layered silicate nanoclay on the dynamic viscoelastic properties of thermoplastic polyurethane nanocomposites. *Applied Clay Science* **2011**, 52 (3), 312-321.
10. Güllü, A.; Özdemir, A.; Özdemir, E., Experimental investigation of the effect of glass fibres on the mechanical properties of polypropylene (PP) and polyamide 6 (PA6) plastics. *Materials & design* **2006**, 27 (4), 316-323.

## Korean Abstract

### 초 록

최근, 제조 산업에서 경량화, 열적/기계적 안정성 등 물성 개선을 위한 신소재 개발이나 새로운 공법 개발이 연구되고 있다. 이는 새로운 구조 설계, 성형 공정 및 재료 개발 등 방식을 통해 실현될 수 있다. 그 중 기존 무거운 소재를 경량 소재로 교체하는 것이 가장 효과적인 방법이다. 따라서 탄소섬유복합재료가 좋은 대안으로 떠오르고 있고, 이에 대한 연구와 수요도 급격히 증가하고 있으며 현재 항공우주, 자동차, 윈드블레이드, 스포츠 등 다양한 산업에서 사용되고 있다. 본 연구는 주로 자동차 경량화를 진행하는데 중요한 역할을 하는 탄소섬유 복합재료 차륜의 제조과정에 대한 연구를 진행하였다. 탄소섬유 복합재료 차륜은 고분자 성형 공정 중 가장 대표적인 수지 이송 성형(RTM)과 사출 성형(IM)으로 제조되었으며, 수지 이송 성형 공정에서는 먼저 수지의 유동성을 예측하고, 공정 조건을 최적화하기 위해 시뮬레이션을 진행했고 해석 결과를 기반으로 실제 제품을 제조하여 실차 테스트까지 통과 하였다. 사출 성형 공정에서는 충전 과정에서의 수지 유동과 제품의 변형을 예측하기 위해 3 차원(3D) 수치 해석을 진행하였다. 또한 시편을 제작해 실제 차륜의 성형성도 확인하였다. 이는 실제 사출 성형을 통해 차륜을 제조하는데 필요한 가이드라인을 제시하였다.

제 2 장에서는 수지 이송 성형 공정을 통한 차륜 제조에 대한 과정에 대해 서술하였다. 우선, 직물의 투과율 계수 텐서에 대한 예측과 측정을 진행하였다. 투과율 계수는 수지 이송 성형 공정에서 가장 중요한 핵심 재료 물성이다. Creeping flow 에 대한 유동 해석을 수행하여 단위셀의 속도장과 압력장에 대한 결과를 얻었으며, Darcy 의 법칙을 이용하여 투과성 계수를 계산하였다. NCF 직물의 단위 셀을 추출하고, 축 방향, 가로 방향, 두께 방향 등 세가지 방향에 대한 투과율계수를 예측하였다. Shifting 영향을 고려하여 보다 현실적인

투과율 계수 값을 얻었다. 투과율 계수 측정 실험도 진행하였으며 예측 결과와 섬유 부피, 섬유 패턴 및 적층 구조에 대해 비교하였다. 다음, 3 차원 수치 이송 성형 유동 해석을 수행하여 복잡한 금형에서의 수치 흐름을 예측하였다. 19 인치 차륜은 탄소 섬유 프리폼과 에폭시 수지를 사용하여 설계 및 제작되었다. void 를 최소화하기 위한 공정 최적화를 진행하였다. 수치와 실험 결과가 서로 잘 맞아떨어졌고, 해석으로 공정 최적화를 진행하여 제품 품질이 크게 향상되었다. 마지막으로 열, 기계, 점탄성 및 구조 분석을 수행하여 최종 개발된 차륜의 다양한 물성을 파악하였다. 벤치마크 제품과 문헌 값을 비교하여 물성의 신뢰성을 높였다. 그 결과, 다양한 기준을 만족시키는 탄소섬유 복합재료 차륜이 성공적으로 개발되고 제작되었다.

제 3 장에서는 열가소성 수치로 탄소섬유 복합재료 차륜을 제조하기 위한 재료 설계를 먼저 수행하였다. 수지를 40wt% 탄소섬유가 포함되어있는 폴리아미드 6(PA6)로 선택한 후 복잡한 형상의 탄소섬유 복합재료 차륜의 사출 성형에 대해 해석을 진행하였다. 형상이 사출 성형에서 흔히 볼 수 있는 단순한 형태가 아니라 원통형으로 되어있고 두께도 복잡한 형상이므로 diaphragm gate 를 사용하였고 sprue, gate, runner 의 크기와 모양을 형상에 맞게 설계하였다. 충전 시 수치 유동 흐름 및 탈형 후 제품의 변형을 수치적으로 예측하였다. 또한 충전 시간을 최적화하고 게이트 고화 시간을 확인하였다. 부품의 변형을 줄이고 기계적 물성을 개선하기 위해 insert 사출 성형도 고려되었다. Insert 사출 성형 부분은 압력, 섬유 방향, 변형, 탄성계수 및 잔류응력분포 측면에서 평가되었다. Insert 를 적용했을 때 부품의 변형이 현저하게 줄어드는 결과를 확인하였다. 추가로, 실제 제조 공정의 가능성을 보여주기 위해 시편을 제작하였고 열적, 기계적 및 점탄성 분석과 같은 물성을 수치 이송 성형으로 제조된 제품과 동일하게 측정하였다. 실제 사출 성형의 제조 가능성은 수치 이송 성형 공정에서 제조한 제품과 비교하여 검증되었다.

**주요어:** 탄소섬유 복합재료, 차륜, 수지이송성형, 투과율 계수, Shifting 효과, void 예측, 수치 해석, 사출성형, 잔류응력.

**학 번:** 2013-22473